

1 **Nonstructural protein 1 of SARS-CoV-2 is a potent pathogenicity factor**
2 **redirecting host protein synthesis machinery toward viral RNA.**

3

4 Shuai Yuan^{1,6}, Lei Peng^{2,4,6}, Jonathan J. Park^{2,4}, Yingxia Hu¹, Swapnil C. Devarkar¹,
5 Matthew B. Dong^{2,4}, Shenping Wu⁵, Sidi Chen^{2,4*}, Ivan Lomakin^{3*} & Yong Xiong^{1,7*}

6

7 ¹ Department of Molecular Biophysics and Biochemistry, Yale University, New Haven, CT, USA.

8 ² Department of Genetics, Yale University School of Medicine, New Haven, CT, USA

9 ³ Department of Dermatology, Yale university school of medicine, New Haven, CT, USA

10 ⁴ Systems Biology Institute, Yale University, West Haven, CT, USA.

11 ⁵ Department of Pharmacology, Yale University, West Haven, CT, USA.

12 ⁶ These authors contributed equally

13 ⁷ Lead contact

14

15

16 *Correspondence: sidi.chen@yale.edu (S.C.), ivan.lomakin@yale.edu (I.L.), yong.xiong@yale.edu

17 (Y.X.)

18

19 **Summary**

20 The COVID-19 pandemic affects millions of people worldwide with a rising death toll.
21 The causative agent, severe acute respiratory syndrome coronavirus 2 (SARS-CoV-2),
22 uses its nonstructural protein 1 (Nsp1) to redirect host translation machinery to the viral
23 RNA by binding to the ribosome and suppressing cellular, but not viral, protein synthesis
24 through yet unknown mechanisms. We show here that among all viral proteins, Nsp1
25 has the largest impact on host viability in the cells of human lung origin. Differential
26 expression analysis of mRNA-seq data revealed that Nsp1 broadly alters the
27 transcriptome in human cells. The changes include repression of major gene clusters in
28 ribosomal RNA processing, translation, mitochondria function, cell cycle and antigen
29 presentation; and induction of factors in transcriptional regulation. We further gained a
30 mechanistic understanding of the Nsp1 function by determining the cryo-EM structure of
31 the Nsp1-40S ribosomal subunit complex, which shows that Nsp1 inhibits translation by
32 plugging the mRNA entry channel of the 40S. We also determined the cryo-EM
33 structure of the 48S preinitiation complex (PIC) formed by Nsp1, 40S, and the cricket
34 paralysis virus (CrPV) internal ribosome entry site (IRES) RNA, which shows that this
35 48S PIC is nonfunctional due to the incorrect position of the 3' region of the mRNA.
36 Results presented here elucidate the mechanism of host translation inhibition by SARS-
37 CoV-2, provide insight into viral protein synthesis, and furnish a comprehensive
38 understanding of the impacts from one of the most potent pathogenicity factors of
39 SARS-CoV-2.

40

41

42 **Keywords**

43 SARS-CoV-2, Nsp1, cellular viability, transcriptome alteration, cryo-EM, translation
44 inhibition mechanism

45

46 **Highlights**

47 ORF screen identified Nsp1 as a major cellular pathogenicity factor of SARS-CoV-2

48 Nsp1 broadly alters the gene expression programs in human cells

49 Nsp1 inhibits translation by blocking mRNA entry channel

50 Nsp1 prevents physiological conformation of the 48S PIC

51

52 **Introduction**

53 SARS-CoV-2, which causes the worldwide COVID-19 pandemic affecting millions of
54 people, belongs to the β -coronaviruses (Coronaviridae Study Group of the International
55 Committee on Taxonomy of, 2020). The virus contains a positive-sense and single-
56 stranded RNA that is composed of 5'-UTR, two large overlapping open reading frames
57 (ORF1a and ORF1b), structural and accessory protein genes, and 3'-poly-adenylated
58 tail (Lim et al., 2016). Upon entering the host cells, ORF1a and ORF1b are translated
59 and proteolytically processed by virus-encoded proteinases to produce functional
60 nonstructural proteins (Nsps) that play important roles in the viral infection and RNA
61 genome replication (Masters, 2006). Nsp1 is the first viral gene encoded by ORF1a
62 (Figure 1A) and is among the first proteins to be expressed after infection (Ziebuhr,
63 2005). It was shown that human SARS-CoV and group 2 bat coronavirus Nsp1 plays a
64 key role in suppressing the host gene expression (Kamitani et al., 2006; Narayanan et
65 al., 2008; Tohya et al., 2009). SARS-CoV Nsp1 has been shown to inhibit host gene
66 expression using a two-pronged strategy. Nsp1 targets the 40S ribosomal subunit to
67 stall the translation in multiple steps during initiation of translation and also induces an
68 endonucleolytic cleavage of host RNA to accelerate degradation (Kamitani et al., 2009;
69 Lokugamage et al., 2012). Nsp1 therefore has profound inhibitory effects on the host
70 protein production, including suppressing the innate immune system to facilitate the viral
71 replication (Narayanan et al., 2008) and potentially long-term cell viability consequences.
72 Intriguingly, viral mRNA overcomes this inhibition by a yet unknown mechanism, likely
73 mediated by the conserved 5' UTR region of viral mRNA (Huang et al., 2011; Tanaka et
74 al., 2012). Taken together, Nsp1 acts as an important factor in viral lifecycle and

75 immune evasion, and may be an important virulence factor causing the myriad of long-
76 term illnesses of COVID-19 patients. It has been proposed as a target for live
77 attenuated vaccine development (Wathelet et al., 2007; Züst et al., 2007).

78 It is common for RNA viruses to target the initiation step of the host protein
79 translation system to allow expression of the viral proteins (Jan et al., 2016). Most
80 cellular mRNAs have a 5' 7-methylguanosine (m7G) cap structure, which is essential for
81 mRNA recruitment to the 43S preinitiation complex (PIC) through interaction with the
82 translation initiation factor (eIF) eIF4F. 43S PIC is formed by the 40S ribosomal subunit,
83 the ternary complex eIF2-GTP-Met-tRNA_i^{Met}, and the multi-subunit initiation factor eIF3.
84 Binding of the 43S PIC to the m7G-cap results in the loading of the mRNA in the mRNA-
85 binding channel of the 40S to form the 48S PIC, and scanning of the mRNA from 5' to 3'
86 direction under control of eIF1A and eIF1, until the initiation codon AUG is placed in the
87 P site of the 40S. Base pairing of Met-tRNA_i^{Met} with AUG results in conformational
88 changes in the 48S PIC for joining the large 60S ribosomal subunit to form the 80S
89 ribosome primed for protein synthesis (Hinnebusch, 2014, 2017b; Hinnebusch et al.,
90 2016). With the exception of the cricket paralysis virus (CrPV), which does not require
91 any host's eIFs, all other viruses may target different eIFs to redirect the host
92 translational machinery on their own mRNA (Lozano and Martinez-Salas, 2015; Walsh
93 and Mohr, 2011).

94 We present here data demonstrating that among all viral proteins, Nsp1 causes
95 the most severe viability reduction in the cells of human lung origin. The introduction of
96 Nsp1 in human cells broadly alter the transcriptomes by repressing major gene clusters
97 responsible for protein synthesis, mitochondria function, cell cycle and antigen

98 presentation, while inducing a broad range of factors implicated in transcriptional
99 regulation. We further determined the cryo-EM structures of the Nsp1-40S complex with
100 or without the CrPV IRES RNA, which reveal the mechanism by which Nsp1 inhibits
101 protein synthesis and regulates viral protein production. These results significantly
102 advance our understanding of the Nsp1-induced suppression of host gene expression,
103 the potential mechanisms of SARS-CoV-2 translation initiation, and the broad impact of
104 Nsp1 as a comorbidity-inducing factor.

105

106 **Results**

107 **SARS-CoV-2 open reading frame (ORF) screen identifies Nsp1 as a major viral** 108 **factor that affects cellular viability**

109 A recent study has mapped the interactome of viral protein to host cellular components
110 in human HEK293 cells (Gordon et al., 2020), suggesting that these viral proteins might
111 have diverse ways of interacting or interfering with the fundamental cellular machineries
112 of the host cell. We generated a non-viral over-expression vector (pVPSB) for
113 introduction of viral proteins into mammalian cells and testing their effect on cells
114 (Figure 1B). We first confirmed that the positive control GFP can be introduced into
115 virtually all cells at 100% efficiency, using flow cytometry analysis. We cloned 28 viral
116 proteins (27 of the 29 viral proteins and Nsp5 C145A mutation) as open reading frames
117 (ORFs) into this vector and introduce them into human cells by transfection. We chose
118 to first test H1299, an immortalized cancer cell line of human lung origin. Although
119 H1299 cells are not primary lung epithelial cells, they have been utilized as a cellular
120 model to study SARS-CoV, MERS and SARS-CoV-2 (Hoffmann et al., 2020; Wong et al.,

121 2015).

122 We introduced all 28 cloned ORFs individually in parallel to conduct a mini-
123 screen of viral proteins' effect on the viability of H1299 cells (Figures 1B and 1C). We
124 measured cell viability in two time points, 48 and 72 hours (h) post transfection.
125 Unexpectedly, we found Nsp1 as the sole "hit" with significant effect on cell viability at
126 both time points (Figure 1C). To validate the viability observations with increased
127 sensitivity, we generated an H1299 cell line with a constitutive firefly luciferase reporter
128 (H1299-PL), and confirmed that GFP can also be introduced into this cell line at near
129 100% efficiency (Figures S1A-C). We performed validation experiments, again with all
130 28 ORFs along with vector control, at 3 different time points (24, 48 and 72h). Across all
131 three time points, Nsp1-transfected H1299 cells have dramatically reduced luciferase
132 signal, an approximation of cell numbers (Figure 1D). We further repeat the same
133 experiments with the Vero E6 cell line, an African monkey (*Cercopithecus Aethiops*)
134 kidney derived cell line, commonly used in SARS-CoV-2 cellular studies (Blanco-Melo et
135 al., 2020; Hoffmann et al., 2020; Kim et al., 2020; Zhou et al., 2020). Consistently, we
136 observed a robust reduction of cellular viability in Vero E6 cells transfected with Nsp1
137 across all 3 time points (Figure S1D). These data revealed that among all SARS-CoV-2
138 proteins, Nsp1 has the largest detrimental effect on cell viability in H1299 and Vero E6
139 cells.

140

141 **Nsp1 mutants abolish cellular viability phenotype**

142 To ensure that the observed reduction of cell viability is indeed from expression of
143 functional Nsp1, we tested three different mutants of Nsp1, including a truncation

144 mutation after residues 12 (N terminal mutant) and two double mutations that have been
145 reported to ablate the activity of the highly homologous SARS-CoV Nsp1 (Wathelet et
146 al., 2007). The point mutations include Nsp1 mutant³ that has R124/K125 replaced with
147 S124/E125 (R124S/K125E) and Nsp1 mutant⁴ that has N128/ K129 replaced with
148 S128/E129 (N128S/K129E). We performed cellular viability assays with wild-type (WT)
149 Nsp1 along with all three of its mutants. In both H1299-PL and Vero E6-PL cells, we
150 again observed that introduction of Nsp1 into cells significantly reduced cell viability
151 along 24, 48, and 72 hours post electroporation (Figures 1E and S1E). Each of the
152 three mutants (truncation, R124S/K125E and N128S/K129E) reverted this phenotype to
153 the vector control level, fully abolishing the cytotoxic effect of Nsp1 (Figures 1E and
154 S1E). These results confirmed that functional Nsp1, but not its loss-of-function mutants,
155 induce reduction of cellular viability when overexpressed in the two mammalian cell
156 lines.

157 We further tested if Nsp1 expression also leads to cell death. We introduced
158 Nsp1 into H1299 cells, along with controls of empty vector and several other viral
159 proteins (Nsp2, Nsp12, Nsp13, Nsp14, ORF9b, and Spike), and measured cellular
160 apoptosis at 48h post electroporation by flow cytometry analysis of cleaved Caspase 3
161 staining. We found that introduction of Nsp1, but not other viral proteins, induced
162 apoptosis in H1299 cells (Figure S1F). To ensure the cellular apoptosis effect is indeed
163 from expression of functional Nsp1 protein, we performed the same apoptosis assay
164 with Nsp1 and the three non-functional mutants described above. Consistently, only
165 wild-type (WT) Nsp1 induced apoptosis in H1299-PL cells, whereas the three mutants
166 did not (Figure S1G). Replicates of this cleaved Caspase 3 flow assay with the

167 truncation mutation of Nsp1 confirmed that WT Nsp1, but not the loss-of-function
168 truncation mutant, induced apoptosis in H1299-PL cells (Figures 1F and 1G).

169

170 **Transcriptome profiling of Nsp1-overexpressed cells**

171 To unbiasedly investigate the global gene expression changes induced by Nsp1 or its
172 loss-of-function mutant form, we performed transcriptome profiling. We first confirmed
173 that Nsp1 is indeed over-expressed in host cells by qPCR using a custom-designed
174 NSP1-specific probe, at both 24 and 48 hours post electroporation (Figure 2A). We then
175 electroporated in quadruplicates for each of Nsp1, its truncation mutant, or vector
176 control plasmid into H1299-PL cells, and collected samples 24 hours post
177 electroporation for mRNA-seq. We collected 24h instead of 48h or 72h samples in order
178 to capture the earlier effect of Nsp1 on cellular transcriptome. We mapped the mRNA-
179 seq reads to the human transcriptome and quantified the expression levels of annotated
180 human transcripts and genes (Table S3). Principle component analysis showed clear
181 grouping and separation of WT Nsp1, mutant Nsp1, or vector control groups (Figure 2B),
182 confirming the overall quality of the Nsp1 mRNA-seq dataset.

183 Differential expression analysis revealed broad and potent gene expression
184 program changes induced by Nsp1 (Figure 2C; Table S3 and S4), with 5,394 genes
185 significantly downregulated and 3,868 genes significantly upregulated (FDR adjusted q
186 value < 0.01). To examine the highly differentially expressed genes, we used a highly
187 stringent criteria (FDR adjusted q value < 1e-30), and identified 1,245 highly significantly
188 downregulated genes (top NSP1 repressed genes) and 464 highly significantly
189 upregulated genes (top Nsp1 induced genes) (Figure 2C; Table S3 and S4). In sharp

190 contrast, Nsp1 truncation mutant and the vector control showed no differential
191 expression in the transcriptome, even when using the least stringent criteria (FDR
192 adjusted q value < 0.05) (Figures S2A-B; Table S3 and S4). These data revealed that
193 Nsp1 alone can cause major alterations broadly in the transcriptome shortly (24h) after
194 its introduction into host cells, consistent with its cell viability phenotype (Figure 1).

195

196 **Enriched pathway analysis on differentially expressed gene sets revealed strong** 197 **signatures of cellular transcriptome alterations by Nsp1**

198 We globally examined the highly differentially expressed genes as a result of Nsp1
199 expression. To understand what these genes represent as a group, we performed
200 DAVID clustering and biological processes (BP) analysis on the 1,245 top Nsp1-
201 repressed genes and the 464 top Nsp1-induced genes, respectively (Figure 2D; Table
202 S4). Enriched pathways in the top Nsp1-repressed genes showed that the most
203 significant gene ontology groups include functional annotation clusters of ribosomal
204 proteins and translation related processes, such as terms of ribonucleoprotein (RNP)
205 (Hypergeometric test, FDR-adjusted q = 6.30e-57), ribosomal RNA processing (q =
206 2.03e-28), and translation (q = 3.93e-28). Highly enriched Nsp1-repressed genes also
207 include the clusters of mitochondria function and metabolism (most terms with q < 1e-15)
208 and cell cycle and cell division (most terms with q < 1e-10), consistent with the reduced
209 cell viability phenotype. Other intriguing enriched Nsp1-repressed pathways include
210 ubiquitin/proteasome pathways and antigen-presentation activities, as well as mRNA
211 processing. We further performed gene set enrichment analysis (GSEA) that takes into
212 consideration both gene set and ranks of enrichment, and the results largely validated

213 the DAVID findings, with highly similar strongly enriched pathways (Figures 3A and
214 S2C). Analysis of highly differentially expressed genes between Nsp1 vs. Nsp1 mutant
215 showed results virtually identical to those of Nsp1 vs. vector (Figures S2A-B, Table S4).

216 We then examined the expression levels of the highly differentially expressed
217 genes in the context of enriched pathways in Nsp1, mutant Nsp1, or vector control
218 plasmid in H1299-PL cells. As shown in the heatmaps (Figure 3B), over 70 genes
219 involved in translation are strongly repressed upon introduction of Nsp1, including the
220 RPS, RPL, MRPS, MRPL family members, along with other translational regulators
221 such as *AKT1*. The repression effect on these genes is completely absent in the Nsp1
222 mutant group (Figure 3B). The strong repression effect also hit multiple members of the
223 gene families involved in mitochondria function, such as the COX, NUDFA, NUDFB and
224 NUDFS families (Figure 3C). Consistent with the cellular phenotypes, Nsp1 also
225 repressed a large number of mitotic cell cycle genes, including members in the CDK,
226 CDC and CCNB families, components of the centrosome, the anaphase promoting
227 complex and various kinases (Figure 3D). While part of the signal may be driven by
228 ribosomal and/or proteosomal genes, multiple genes involved in the mRNA processing
229 and/or nonsense-mediated decay nevertheless are significantly repressed by
230 Nsp1 (Figures S2D-E). Interestingly, DAVID BP enrichment analysis of Nsp1-repressed
231 genes also scored the antigen presentation pathway, mostly proteasome components
232 along with several MHC-I component members (Figure 3E). Concordantly, Nsp1-
233 repressed genes are also enriched in the ubiquitination and proteasome degradation
234 pathways (Figure S2F).

235 On the other hand, genes highly induced by Nsp1 hit a broad range of factors

236 implicated in transcriptional regulation, such as unfolded protein response regulators
237 (*ATF4*, *XBP1*), FOX family transcription factors (TFs) (*FOXK2*, *FOXE1*, *FOXO1*,
238 *FOXO3*), Zinc finger protein genes (*ZFN217*, *ZFN567*), KLF family members (*KLF2*,
239 *KLF10*), SOX family members (*SOX2*, *SOX4*), Homeobox genes (*HOXD9*, *HOXC8*,
240 *HOXD13*), GATA TFs (*GATAD2B*, *GATA6*), dead-box protein genes (*DDX5*, *DHX36*),
241 cell fate regulators (*RUNX2*, *CREBRF*, *LIF*, *JUNB*, *ELK1*, *JAG1*, *SMAD7*, *BCL3*,
242 *EOMES*); along with certain epigenetic regulators of gene expression such as the
243 SWI/SNF family members *ARID1A*, *ARID1B*, *ARID3B*, and *ARID5B* (Figure 3F).
244 Interestingly, highly upregulated genes are also slightly enriched in the MAPK/ERK
245 pathway, where Nsp1 expression induces multiple DUSP family members (Figure 3G).
246 The upregulated genes also include several KLF family members related to the process
247 of cellular response to peptide (Figure S2G). Again, the induction effect on these genes
248 is completely abolished in the Nsp1 mutant group (Figures 3F and 3G). These data
249 together showed that Nsp1 expression broadly and significantly altered multiple gene
250 expression programs in the host H1299-PL cells.

251

252 **Cryo-EM structure reveals Nsp1 is poised to block host mRNA translation.**

253 To elucidate the mechanism of translation inhibition by Nsp1, we determined the cryo-
254 EM structure of rabbit 40S ribosomal subunit complex with Nsp1 at 2.7 Å resolution
255 (Table 1, Figures S3 and S4). The quality of the cryo-EM map allowed us to
256 unambiguously identify Nsp1 that binds to the head and the body domains of the 40S
257 around the entry to the mRNA channel (Figure 4). The density observed in the mRNA
258 entry channel enabled us to build an atomic model for the C-terminal domain of Nsp1

259 (C-Nsp1, amino acids (aa) 145-180) (Figure 4A). C-Nsp1 comprises two α -helices (α 1,
260 aa 154-160; α 2, aa 166-179) and two short loops (aa 145-153 and 161-165), which
261 blocks the mRNA entry channel (Figure 4B). Besides the α -helices in the mRNA
262 channel, extra globular density between the ribosomal protein uS3 and rRNA helix h16
263 is observed at a lower contour level, whose dimensions roughly matched the N-terminal
264 domain of Nsp1 (aa: 13-127, N-Nsp1, PDB:2HSX) (Almeida et al., 2007) (Figure 4C).
265 However, N-Nsp1 does not appear to be stably bound to the 40S and the low local
266 resolution of the cryo-EM map in this region did not allow for an atomic model for the N-
267 Nsp1.

268 C-Nsp1 bridges the head and body domains of the 40S ribosomal subunit
269 through extensive electrostatic and hydrophobic interactions with the ribosomal proteins
270 uS3 of the head, uS5 and eS30 and helix h18 of the 18S rRNA in the body (Figure 5A).
271 The buried surface area of interaction between C-Nsp1 and the 40S ribosomal subunit
272 is $\sim 1,420 \text{ \AA}^2$. The negatively charged residues D152, E155 and E159 of C-Nsp1 interact
273 with the positively charged residues R117, R116, R143 and K148 of uS3, respectively
274 (Figure 5B). In addition, the positively charged surface of C-Nsp1 binds to the negatively
275 charged rRNA backbone of h18 (Figure 5C). K164 of Nsp1 inserts into the negatively
276 charged pocket formed by the backbone of G625 and U630 of the rRNA h18. H165 of
277 Nsp1 stacks with the base of U607 of h18, and R171 and R175 of C-Nsp1 interact with
278 the negatively charged patch formed by G601, A604, G606 and U607 of h18 (Figure
279 5C). Besides electrostatic contacts, a large hydrophobic patch of C-Nsp1, which is
280 formed by F157, W161, L173 and L177, interacts with a complimentary hydrophobic
281 patch on uS5 formed by V106, I109, P111, T122, F124, V147 and I151 (Figure 5D).

282 Intriguingly, K164 and H165 of Nsp1, which have been shown to play an important role
283 in host translation inhibition, are conserved only in the betacoronaviruses (beta-CoVs)
284 (Figure 5E). In addition, the other Nsp1 residues interacting with the h18 of rRNA are
285 also conserved only among the beta-CoVs (Figure 5E). This sequence conservation
286 indicates that the hydrophobic interactions between C-Nsp1 and uS5 are likely universal
287 in both alpha- and beta-CoVs, while the electrostatic interactions between C-Nsp1 and
288 the h18 of the 18S rRNA are conserved only in the beta-CoVs.

289 The extensive interactions result in C-Nsp1 plugging the mRNA entry channel,
290 which prevents the loading and accommodation of the mRNA (Figure 4B), providing a
291 structural basis for the inhibition of host protein synthesis by Nsp1 of SARS-CoV-2 and
292 SARS-CoV reported previously (Kamitani et al., 2009; Kamitani et al., 2006). Because
293 Nsp1 molecules of both viruses share 84% amino acid sequence identity, they likely act
294 by the same mechanism (Figures 5A and 5E). It was shown that K164 and H165 of
295 SARS-CoV Nsp1 KH motif are essential for the suppression of host protein synthesis
296 (Kamitani et al., 2009). In our structure the motif provides critical interactions with helix
297 h18, anchoring Nsp1 to the 18S rRNA (Figure 5C). These interactions constitute ~15%
298 of the overall C-Nsp1-40S ribosome interacting surface, which explains the detrimental
299 effect of K164A and H165A mutations on inhibition of host protein synthesis.

300

301 **Nsp1 locks the 40S in a conformation incompatible with mRNA loading and**
302 **disrupts initiation factor binding**

303 The ribosomal protein uS3 is conserved in all kingdoms. Together with h16, h18 and
304 h34 of 18S rRNA it constitutes the mRNA-binding channel and the mRNA entry site

305 (Graifer et al., 2014; Hinnebusch, 2017a). It has been shown that uS3 interacts with the
306 mRNA and regulates scanning-independent translation on a specific set of mRNAs
307 (Haimov et al., 2017; Sharifulin et al., 2015). Interestingly, conserved residues R116 and
308 R117 of uS3, which are crucial for stabilizing mRNA in the entry channel and
309 maintaining 48S PIC in the closed conformation, are interacting with D152, E155 of
310 Nsp1 in our structure (Dong et al., 2017; Hinnebusch, 2017a) (Figure 5B). Moreover, the
311 conformation of the 40S ribosomal subunit in Nsp1-40S complex is similar to that of
312 'closed state' of 48S PIC with initiator tRNA locked in the P site and the latch closed
313 (Lomakin and Steitz, 2013), which is incapable of mRNA loading. The distance between
314 G610 (h18) and GLN179 (CA, uS3) is shortened from 19.4 Å in the 'open state' 48S PIC
315 (PDB:3JAJ) to 15.8 Å in Nsp1-40S ribosomal complex, which is similar to the distance
316 of 15.0 Å in the closed state 48S PIC (PDB:4KZZ) (Figure 5F). This shows that Nsp1
317 not only plugs the mRNA entry channel, but also keeps the 40S subunit in a
318 conformation that is incompatible with mRNA loading.

319 The known structure of the N-terminal domain of SARS-CoV (N-Nsp1) (Almeida
320 et al., 2007) (PDB ID: 2HSX) can be docked into the extra globular density between uS3
321 and rRNA helix h16 in the cryo-EM map (Figure 6A). This potential interaction between
322 N-Nsp1 and uS3 covers most of the uS3 surface on the solvent side, including the
323 GEKG loop of uS3 (aa: 60-63) that corresponds to the consensus GXXG loop
324 conserved in the KH domains of various RNA-binding proteins (Babaylova et al., 2019b;
325 Graifer et al., 2014). Mutation of the GEKG loop to alanines does not abrogate the
326 ability of the 40S to bind mRNA and form 48S preinitiation complex (PIC). Instead, it
327 results in the formation of aberrant 48S PIC that cannot join the 60S ribosomal subunit

328 and assemble the 80S initiation complex (Graifer et al., 2014). Peculiarly, binding of
329 SARS-CoV Nsp1 to the ribosome led to the same effect (Kamitani et al., 2009). We
330 hypothesize that Nsp1 may prevent the formation of physiological conformation of the
331 48S PIC induced by uS3 interaction with translation initiation factors, such as the j
332 subunit (eIF3j) of the multi-subunit initiation factor eIF3 (Babaylova et al., 2019b; Cate,
333 2017; Sharifulin et al., 2016). The eIF3 complex plays a central role in the formation of
334 the translation initiation complex (Cate, 2017; Hinnebusch, 2014). eIF3j alone binds to
335 the 40S ribosomal subunit and stabilizes the interaction with eIF3 complex (Fraser et al.,
336 2004b; Sokabe and Fraser, 2014). The binding site of eIF3j to 40S subunit is not
337 precisely determined. Cryo-EM and biochemical studies mapped it onto the mRNA
338 binding channel of the 40S, extending from the decoding center toward the mRNA entry
339 region, including the GEKG loop of uS3 (Aylett et al., 2015; Fraser et al., 2007; Hershey,
340 2015) (Figure 6B).

341 We tested if Nsp1 can compete with eIF3j for the binding to the 40S ribosomal
342 subunit. The result showed that Nsp1 indeed significantly reduces the binding between
343 eIF3j and the 40S (Figure 6C). The binding competition of eIF3j and Nsp1 to the 40S
344 was tested at different concentrations. There is little eIF3j binding to the 40S when the
345 concentration of eIF3j is equal or lower than that of Nsp1, and residual eIF3j binding
346 was observed only when its concentration is higher than that of Nsp1 (Figures 6C and
347 S5). By contrast, the binding of Nsp1 to the 40S is not affected even when eIF3j is in
348 excess. These results indicate that Nsp1 disrupts the binding of eIF3j to the 40S,
349 potentially by shielding the access to uS3 and the mRNA binding channel and/or by
350 making the conformation of the 40S unfavorable for eIF3j interaction.

351

352 **Nsp1 prevents physiological conformation of the 48S PIC**

353 It was shown previously that binding of SARS-CoV Nsp1 to the 40S ribosomal subunit
354 does not inhibit 48S PIC formation, but it suppresses 60S subunit joining (Kamitani et al.,
355 2009). To understand the effect of Nsp1 of SARS-CoV-2 on 48S PIC, we determined a
356 3.3 Å resolution cryo-EM structure of Nsp1 bound to the 48S PIC assembled with the
357 cricket paralysis virus (CrPV) internal ribosome entry site (IRES) (Figures 6D, S6, and
358 S7). CrPV IRES has become an important model for studies of the eukaryotic ribosome
359 during initiation, as it is able to directly recruit and assemble with 40S or 80S ribosome
360 without requiring any eIFs (Martinez-Salas et al., 2018). It was shown that SARS-CoV
361 Nsp1 inhibits translation of the CrPV IRES RNA (Kamitani et al., 2009). We first
362 examined whether Nsp1 affects binding of the IRES RNA to the 40S ribosomal subunit.
363 The result shows that Nsp1 and CrPV IRES can bind 40S ribosomal subunit
364 simultaneously (Figure S6). Consistently, both C-Nsp1 and the CrPV IRES can be seen
365 in the cryo-EM map (Figure 6D), where the Nsp1 C-terminal domain is inserted in the
366 RNA entry channel in the same way as in the Nsp1-40S complex without the IRES RNA
367 (Figures 4A and 4B). The local environment of C-Nsp1 in the ribosome RNA entry
368 channel with or without the IRES RNA is quite similar. No conformational changes were
369 observed for C-Nsp1, protein uS5 and rRNA h18, however, the head of the 40S subunit
370 is moved by about 2.8 Å (Figure 6D) (discussed more below).

371 We fitted the high resolution structure of the CrPV IRES from the yeast 40S-CrPV
372 IRES complex (Murray et al., 2016) (PDB: 5IT9) into our cryo-EM map. Importantly, the
373 pseudoknot I (PKI) domain of the CrPV IRES, which is a structural mimic of the

374 canonical tRNA-mRNA interaction, is not seen in the cryo-EM map, suggesting that it is
375 dislodged from the 40S in the presence of Nsp1 (Figure 6E). Consistently, there would
376 be a clash between Nsp1 C-terminal domain and the 3' region of the IRES RNA in the
377 previously observed conformation bound to the 40S (Murray et al., 2016) (Figure 6E).
378 The conformation of the 40S head in the Nsp1-40S-CrPV IRES complex is different
379 from that in the Nsp1-40S complex (Figure 6F). The head in the Nsp1-40S-CrPV IRES
380 complex is in somewhat intermediate conformation compared to the Nsp1-40S and the
381 40S-CrPV IRES complexes (Figure 6F). This suggests that the Nsp1-40S interactions
382 resist the conformational changes induced by the IRES for translation initiation.
383 Conformational changes of the head domain of the 40S subunit play important role in
384 the mRNA loading and recruitment of the 60S subunit to form the 80S ribosome. Nsp1
385 limits the rotation of the head, which may have profound consequences interfering with
386 the joining of the 60S subunit and the formation of the 80S initiation complex.

387

388 **Discussion**

389 SARS-CoV-2 infection causes a series of damages to the human body, often leading to
390 long-term illnesses (Grasselli et al., 2020). However, the cellular phenotypes and the
391 relative contributions of individual viral proteins are not clearly understood. While viral
392 infection is a complex process involving multiple components, certain viral proteins are
393 often in high abundance in cells during active viral replication (Astuti and Ysrafil, 2020;
394 Yoshimoto, 2020). Therefore, understanding the effects of each individual viral protein
395 on the cells provides important insights on the cellular impacts of viral infection. Using a
396 reductionist approach, we tested the gross cellular effect of expressing all the SARS-

397 CoV-2 proteins individually. Among all 27 viral proteins, Nsp1 showed the strongest
398 deleterious effect on cell viability in H1299 cells of human lung epithelial origin. This is in
399 concordance with previous observations from related coronaviruses, such as mouse
400 hepatitis virus (MHV) Nsp1 being a major pathogenicity factor strongly reducing cellular
401 gene expression (Zust et al., 2007), and SARS-CoV Nsp1 inhibiting interferon (IFN)-
402 dependent signaling and having significant effects on cell cycle (Wathelet et al., 2007). A
403 recent study shows that SARS-CoV-2 Nsp1 shuts down mRNA translation in cells and
404 suppresses innate immunity genes such as *IFNb* and *IL-8*, although these experiments
405 were conducted in HEK293T cells of kidney origin, and only a small number of host
406 genes were tested (Thoms et al., 2020). As an unbiased interrogation of global cellular
407 pathways affected by Nsp1, our transcriptome profiling data and gene set enrichment
408 analysis revealed strong signatures of transcriptomic changes in broad ranges of host
409 genes with several major clusters, providing a comprehensive understanding of the
410 impacts of one of the most potent pathogenicity protein factors of SARS-CoV-2 in
411 human cells of lung origin.

412 Our structure of the SARS-CoV-2 Nsp1 protein bound to the 40S ribosomal
413 subunit establishes a mechanistic basis of the cellular effects of Nsp1, revealing a
414 multifaceted mechanism of inhibition of the host protein synthesis at the initiation stage
415 by the virus. Nsp1 plugs the mRNA channel entry from the position +10 and up, which
416 physically blocks access to the channel by any mRNA (Figure 4B). This is consistent
417 with the result obtained from similar structural studies (Thoms et al., 2020). Moreover,
418 Nsp1 interacts with the ribosomal protein uS3 of the head domain and uS5 of the body
419 domain of the 40S subunit as well as with the helix h18 of the 18S rRNA, which locks

420 the head domain of the 40S subunit in the closed position. This position is characterized
421 by the closed conformation of the “mRNA entry channel latch” that clams around
422 incoming mRNA (Hinnebusch, 2017b; Lomakin and Steitz, 2013; Passmore et al., 2007).
423 The latch is supposed to be closed during the scanning of the mRNA, keeping mRNA
424 locked in the binding cleft and increasing processivity of the scanning, whereas the
425 open conformation of the latch would facilitate the initial attachment of the 43S PIC to
426 the mRNA (Lomakin and Steitz, 2013). Therefore, when Nsp1 keeps the latch closed it
427 makes impossible for the host mRNA to be loaded. In addition, the N-terminal domain of
428 Nsp1 interacts with the KH-domain of uS3, specifically with its GEKG loop crucial for
429 translation initiation (Figures 6A and 6B) (Babaylova et al., 2019a). We showed that
430 Nsp1 competes with eIF3j for the binding to the 40S subunit (Figure 6C). This allows us
431 to propose that Nsp1 weakens the binding of the eIF3 to the 40S subunit by disrupting
432 uS3-eIF3j interaction. Moreover, accessibility to the GEKG loop of uS3 is required for
433 the functional 48S PIC formation (Babaylova et al., 2019a; Fraser et al., 2004a; Graifer
434 et al., 2014; Sokabe and Fraser, 2014).

435 Our results explain how Nsp1 inhibits protein synthesis; however, how SARS-
436 CoV-2 escapes this inhibition and initiate translation of its own RNA still remains
437 unanswered. The 5'-UTR of SARS-CoV-2 is essential for escaping Nsp1-mediated
438 suppression of translation (Tanaka et al., 2012). Interactions involving the viral 5' UTR
439 presumably result in the “unplugging” of Nsp1 from the 40S ribosome during the
440 initiation of viral translation. In addition, the weakening of eIF3 binding to the 40S
441 subunit is beneficial for translation initiation of some viruses. The hepatitis C virus (HCV)
442 IRES displaces eIF3 from the interface of the 40S subunit to load its RNA in the mRNA

443 binding channel (Hashem et al., 2013; Niepmann and Gerresheim, 2020). HCV IRES
444 interacts with eIF3a, eIF3c and other core subunits of eIF3 to promote formation of the
445 viral 48S PIC (Cate, 2017). The eIF3d subunit of the eIF3 complex can be cross-linked
446 to the mRNA in the exit channel of the 48S PIC, it has its own cap-binding activity which
447 can replace canonical eIF4E dependent pathway and promote translation of selected
448 cellular mRNAs (Lee et al., 2016; Pisarev et al., 2008; Walker et al., 2020). Interestingly,
449 a recent genome-wide CRISPR screen revealed the eIF3a and eIF3d are essential for
450 SARS-CoV-2 infection (Wei et al., 2020). It is possible that SARS-CoV-2 may use an
451 “IRES-like” mechanism involving eIF3 recruitment by 5' UTR to overcome Nsp1
452 inhibition. Binding of 5' UTR may cause conformational change of the 40S head leading
453 to the latch opening, Nsp1 dissociation, viral RNA loading into mRNA binding channel
454 and formation of the functional 80S initiation complex primed for viral protein synthesis.
455 However, the detailed mechanisms of viral escape of Nsp1 inhibition must await for
456 future experimental studies.

457

458 **Acknowledgements**

459 We thank the Yale cryo-EM facilities for assistance with data collection. We thank the
460 Xiong lab and Chen lab members for discussions. We thank Xiaoyun Dai, Lupeng Ye
461 and several others for sharing various plasmids and reagents. We thank the Yale
462 Center for Genome Analysis and Center for Research Computing for providing High-
463 throughput sequencing and computing assistance and resources.

464

465 **Funding**

466 This work was supported by Yale discretionary funds to Y.X. and S.C.

467

468 **Author contributions**

469 S.Y., L.P., S.C., I.L. and Y.X. initiated the project and designed the experiments. S.Y. I.L,
470 and Y.H. produced proteins and 40S ribosomal subunit. S.Y. and S.D. performed
471 binding assays. S.Y. prepared the cryo-EM samples. Y.H. and S.W. carried out cryo-EM
472 data collection. S.Y. and Y.X. did cryo-EM data processing. S.Y., I.L., S.D. and Y.X.
473 analyzed cryo-EM structure. L.P. and M.B.D. performed cellular assays. L.P. and J.J.P.
474 performed and processed mRNA-seq. S.Y., L.P., S.C., I.L. and Y.X. prepared the
475 manuscript. S.C., I.L. and Y.X. jointly supervised the work.

476

477 **Declaration of interests**

478 The authors declare no competing interests.

479

480

481 **Figures**

482

483 **Figure 1. SARS-CoV-2 ORF mini-screen identified Nsp1 as a key viral protein with** 484 **host cell viability effect.**

485 (A) Schematics of viral protein coding frames along SARS-CoV-2 genome. Colored
486 ORFs indicate the ones used in this study, while two ORFs in grey are not (Nsp3
487 and Nsp16).

488 (B) Schematics of molecular and cellular experiments of viral proteins.

489 (C) Scatter plot of SARS-CoV-2 ORF mini-screen for host viability effect in H1299
490 cells, at 48 and 72 hours post ORF introduction. Each dot represents the mean
491 normalized relative viability of host cells transfected with a viral protein encoding
492 ORF. Dash line error bars indicate standard deviations. (n = 3 replicates). Pink
493 color indicates hits with p < 0.05 (one-way ANOVA, with multiple group
494 comparison).

495 (D) Bar plot of firefly luciferase reporter measurement of viability effects of SARS-
496 CoV-2 ORFs in H1299-PL cells, at 24, 48 and 72 hours post ORF introduction (n
497 = 3 replicates).

498 (E) Bar plot of firefly luciferase reporter measurement of viability effects of Nsp1 and
499 three Nsp1 mutants (truncation, mut3: R124S/K125E and mut4: N128S/K129E)
500 in H1299-PL cells, at 24, 48 and 72 hours post ORF introduction (left, middle and
501 right panels, respectively) (n = 3 replicates).

502 (F) Flow cytometry plots of apoptosis analysis of Nsp1 and loss-of-function
503 truncation mutant in H1299-PL cells, at 48 hours post ORF introduction.

504 Percentage of apoptotic cells was gated as cleaved Caspase 3 positive cells.

505 (G) Quantification of flow-based apoptosis analysis of Nsp1 and loss-of-function
506 truncation mutant in H1299-PL cells, at 48 hours post ORF introduction.

507 For all bar plots in this figure: Bar height represents mean value and error bars
508 indicate standard error of the mean (sem). (n = 3 replicates for each group).

509 Statistical significance was accessed by ordinary one-way ANOVA, with multiple
510 group comparisons where each group was compared to empty vector control, with p-
511 values subjected to multiple-testing correction by FDR method. (ns, not significant; *
512 p < 0.05; ** p < 0.01; *** p < 0.001; **** p < 0.0001).

513 See also Figure S1.

514

515

516 **Figure 2. Transcriptome profiling of H1299 cells introduced with NSP1 and NSP1** 517 **truncation mutant by RNA-seq.**

518 (A) Quantitative PCR (qPCR) confirmation of *NSP1* overexpression, at 24 and 48
519 hours post electroporation. (n = 3 replicates).

520 (B) Principle component analysis (PCA) plot of the entire mRNA-seq dataset,
521 showing separation between Nsp1, Vector control and Nsp1 truncation mutant
522 groups, all electroporated into H1299-PL cells and harvested 24 hours post
523 electroporation. RNA samples were collected as quadruplicates (n = 4 each
524 group).

525 (C) Volcano plot of differential expression between of Nsp1 vs Vector Control
526 electroporated cells. Top differentially expressed genes (FDR adjusted q value <

527 1e-100) are shown with gene names. Upregulated genes are shown in orange.
528 Downregulated genes are shown in blue.

529 **(D)** Bar plot of top enriched pathway analysis by DAVID Biological Processes (BP).
530 Nsp1 vs Vector control (top), or Nsp1 vs Nsp1 mutant (top), highly
531 downregulated (left) and upregulated (right) genes are shown ($q < 1e-30$).

532 See also Figure S2

533

534

535 **Figure 3. Highly differentially expressed genes between Nsp1, Vector control and**
536 **Nsp1 mutant group in the context of top major enriched pathways.**

537 **(A)** Gene set enrichment plots of representative enriched pathways by GSEA.

538 **(B-E)** Heatmap of Nsp1 highly repressed genes ($q < 1e-30$) in rRNA processing and
539 translation **(B)**, mitochondria function **(C)**, cell cycle **(D)**, MHC-I antigen presentation
540 processes **(E)**.

541 **(F-G)** Heatmap of Nsp1 highly induced genes ($q < 1e-30$) in *polII* related
542 transcription regulation processes **(F)** and the MAPK/ERK pathway **(G)**.

543 See also Figure S2

544

545

546 **Figure 4. cryo-EM structure of the Nsp1-40S ribosome complex.**

547 **(A)** Overall density of the Nsp1-40S ribosome complex with Nsp1 (green) and 40S.
548 ribosome (gray). Inset shows C-Nsp1 with corresponding density with clear
549 sidechain features. C-Nsp1 α -helices (α_1 , aa 154-160; α_2 , aa 166-179) are
550 labeled.

551 **(B)** Cross section of the C-Nsp1 (green) within the mRNA entry channel. 40S.
552 ribosome is shown in surface and C-Nsp1 is displayed in cartoon.

553 **(C)** Overall density of Nsp1-40S ribosome complex at a lower contour level. Insets.
554 shows the extra globular density with SARS-CoV Nsp1 N-terminal domain
555 (PDB:2HSX, green) fitted. Ribosomal protein uS3 (magenta) and rRNA h16
556 (orange) are shown in cartoon.

557 See also Figures S3 and S4.

558

559

560 **Figure 5. Structural basis of C-Nsp1 and 40S ribosome interaction.**

561 **(A)** Overall structure of the C-Nsp1-40S ribosome complex, with C-Nsp1 (green.
562 surface) and the surrounding protein uS3 (magenta sphere representation), uS5
563 (cyan) and rRNA h18 (orange) highlighted. The inset shows zoomed-in view of
564 C-Nsp1 in cartoon, with the surrounding 40S components in cartoon and surface
565 to illustrate the mRNA entry channel.

566 **(B-D)** Molecular interactions between C-Nsp1 and 40S ribosome components,
567 including uS3 **(B)**, h18 **(C)**, uS5 **(D)**. Left panels: Proteins and rRNA are in the
568 same color as in **(A)** and shown in cartoon, with binding pocket and
569 hydrophobic interface depicted in surface. The interacting residues are shown
570 in sticks. Right panels: The complementary electrostatic surfaces at the
571 interfaces (marked with ovals), colored by electrostatic potential (blue,
572 positively charged; red, negatively charged).

- 573 (E) Alignment of the last 40 residues at Nsp1 C-terminus from beta-CoVs (SARS-
574 CoV-1, SARS-CoV-2, MERS-CoV and MHV) and alpha-CoVs (TGEV, HCoV-
575 229E and HCoV-NL63) coronaviruses. Residues conserved in both alpha- and
576 beta-CoVs are boxed in blue. Residues only conserved in beta-CoVs
577 coronaviruses are with orange boxes. Conserved residues that mediate the
578 interaction with the 40S are marked with red triangles.
- 579 (F) The conformation of the 40S ribosome in the Nsp1-40S complex is similar to the
580 close form in the 48S PIC. Q179 of uS3 (magenta cartoon) is displayed as a
581 sphere. h18 is in cartoon and colored dark yellow (48S closed conformation),
582 orange (Nsp1-40S ribosome complex) and dark green (48S open conformation),
583 with distances to Q179 indicated by the dashes.

584
585

586 **Figure 6. Nsp1 disrupts initiation factor binding and prevents physiological**
587 **conformation of the 48S PIC.**

- 588 (A) The N-terminal domain of Nsp1 covers uS3 surface on the solvent side. The
589 cryo-EM density in this region is shown in blue surface with SARS-CoV Nsp1 N-
590 terminal domain (PDB:2HSX) fitted. uS3 (magenta) is depicted cartoon. The
591 GEKG loop (dark purple) is shown in sphere representation.
- 592 (B) Potential binding region of eIF3j. The putative location of eIF3j is marked in red.
- 593 (C) SDS-PAGE analysis of Nsp1 and eIF3j competition at different concentration
594 ratios (indicated in the top table).
- 595 (D) Overall structure of the Nsp1-40S-CrPV IRES complex. Nsp1 (green) and IRES.
596 (yellow) are presented in surface. The ribosome proteins (slate) and rRNA
597 (orange) are shown in cartoon. The right insets display the conformation change
598 in the Nsp1-binding region (cartoon representation) with or without the IRES.
- 599 (E) The previously reported model of CrPV IRES (PDB: 5IT9, orange cartoon) fitted.
600 to 40S ribosome in the present of Nsp1 (green cartoon). 40S ribosome (slate)
601 and the currently observed IRES (yellow) are presented in surface.
- 602 (F) C-Nsp1 restricts the 40S ribosome head rotation. Superposition of the Nsp1-
603 40S , Nsp1-40S-CrPV IRES and IRES-40S (PDB:5IT9) complexes is shown in
604 cartoon. Zoomed view displays the head rotations represented by selected rRNA
605 regions. C-Nsp1 (green) is displayed in surface.
- 606 See also Figures S5, S6 and S7.

607

608 Supplemental Figures

609 610 **Figure S1. Flow cytometry analysis of cellular effects of SARS-CoV-2 ORFs, Nsp1,** 611 **and Nsp1 mutants, Related to Figure 1.**

- 612 (A) Diagram of example flow gating.
- 613 (B) Flow cytometry plots of GFP expression in H1299 cells, at 48 hours post ORF
614 introduction.
- 615 (C) Flow cytometry plots of GFP expression in H1299-PL cells, at 48 hours post
616 ORF introduction.
- 617 (D) Bar plot of firefly luciferase reporter measurement of viability effects of SARS-
618 CoV-2 ORFs in Vero E6-PL cells, at 24, 48 and 72 hours post ORF introduction
619 (n = 3 replicates).
- 620 (E) Bar plot of firefly luciferase reporter measurement of viability effects of Nsp1 and
621 three Nsp1 mutants (truncation, mut3: R124S/K125E and mut4: N128S/K129E)
622 in Vero E6-PL cells, at 24, 48 and 72 hours post ORF introduction (left, middle
623 and right panels, respectively) (n = 3 replicates).
- 624 (F) Flow cytometry plots of apoptosis analysis of Nsp1 and three Nsp1 mutants
625 (truncation, mut3: R124S/K125E and mut4: N128S/K129E) in H1299-PL cells, at
626 48 hours post ORF introduction. Percentage of apoptotic cells was gated as
627 cleaved Caspase 3 positive cells.
- 628 (G) Flow cytometry plots of apoptosis analysis of several SARS-CoV-2 ORFs (Nsp1,
629 Nsp2, Nsp12, Nsp13, Nsp14, Orf9b and Spike), at 48 hours post ORF
630 introduction, in H1299 cells. Percentage of apoptotic cells was gated as cleaved
631 Caspase 3 positive cells.

632 For all bar plots in this figure: Bar height represents mean value and error bars indicate
633 standard error of the mean (sem). (n = 3 replicates for each group). Statistical
634 significance was accessed by ordinary one-way ANOVA, with multiple group
635 comparisons where each group was compared to empty vector control, with p-values
636 subjected to multiple-testing correction by FDR method. (ns, not significant; * p < 0.05;
637 ** p < 0.01; *** p < 0.001; **** p < 0.0001).

638 639 640 **Figure S2. Additional differential expression and pathway analysis of H1299 Nsp1** 641 **mRNA-seq dataset, Related to Figures 2 and 3**

- 642 (A) Volcano plot of differential expression between of Nsp1 vs Nsp1 mutant
643 electroporated cells. Genes highly differentially expressed (FDR adjusted q
644 value < 1e-100) are shown with gene names. Upregulated genes are shown in
645 orange. Downregulated genes are shown in blue.
- 646 (B) Volcano plot of differential expression between of Nsp1 mutant vs Vector Control
647 electroporated cells. As seen in the plot, no gene in the genome is differentially
648 expressed between these two groups.
- 649 (C) Gene set enrichment plots of additional representative enriched pathways by
650 GSEA.
- 651 (D) Heatmap of Nsp1 highly repressed genes (q < 1e-30) in the mRNA processing
652 and nonsense-mediated decay processes.
- 653 (E) Heatmap of Nsp1 highly repressed genes (q < 1e-30) in the SRP proteins.

654 (F) Heatmap of Nsp1 highly repressed genes ($q < 1e-30$) in the ubiquitination and
655 proteasome degradation processes.

656 (G) Heatmap of Nsp1 highly induced genes ($q < 1e-30$) in the cellular response to
657 peptide processes.

658
659

660 **Figure S3. SDS-PAGE analysis of Nsp1 and 40S ribosome binding, Related to**
661 **Figure 4.** Nsp1 is labeled with an MBP tag. MBP-snap was used as a negative control.

662
663

664 **Figure S4. Data processing of Nsp1-40S ribosome complex cryo-EM dataset,**
665 **Related to Figure 4.**

666 (A) FSC curves of the half-maps from gold standard refinement of the Nsp1-40S
667 ribosome complex (blue) and masked local refinement of the head domain (red).

668 (B-C) Color coded local resolution estimation of the overall complex (B) and local-
669 refined head domain (C).

670
671

672 **Figure S5. SDS-PAGE analysis of Nsp1 and eIF3j competition assay, Related to**
673 **Figure 6.**

674 Concentration ratios are shown in top table. Top gel: Assay with MBP-Nsp1. Bottom gel:
675 Full-length Nsp1 without the MBP tag was used to exclude the tag effect.

676
677

678 **Figure S6. CrPV IRES and Nsp1 can bind to 40S ribosome simultaneously,**
679 **Related to Figure 6.**

680 SDS-PAGE analysis (A) and RNA gel (B) show the binding of Nsp1 and CrPV IRES.

681
682

683 **Figure S7. Data processing of Nsp1-40S-CrPV IRES complex cryo-EM dataset,**
684 **Related to Figure 6.**

685 (A) FSC curves of the half-maps from gold standard refinement of the Nsp1-40S-
686 CrPV IRES complex.

687 (B) Color coded local resolution estimation of the complex.

688
689

690 **Table 1. Cryo-EM data collection, refinement and validation statistics**

691

	Nsp1-40S ribosome (EMDB-xxxx) (PDB xxxx)	Nsp1-40S-CrPV IRES (EMDB-xxxx) (PDB xxxx)
Data collection and processing		
Magnification	81,000	81,000
Voltage (kV)	300	300
Electron exposure (e ⁻ /Å ²)	50	50
Defocus range (μm)	0.5-2.0	0.5-2.0
Pixel size (Å)	1.068	1.068
Symmetry imposed	C1	C1
Initial particle images (no.)	668,695	60,690
Final particle images (no.)	353,927	48,689
Map resolution (Å)	2.7	3.3
FSC threshold.	0.143	0.143
Map resolution range (Å)	2.5-4.5	3.0-5.0
Refinement		
Initial model used (PDB code)	4KZX	4KZX
Model resolution (Å)	2.7	3.3
FSC threshold	0.143	0.143
Model resolution range (Å)		
Map sharpening <i>B</i> factor (Å ²)	88	23
Model composition		
Non-hydrogen atoms	74,976	77,833
Protein residues	4,859	4,837
Ligands (nucleotide)	1,697	1,840
<i>B</i> factors (Å ²)		
Protein	143	144
Ligand (nucleotide)	154	169
R.m.s. deviations		
Bond lengths (Å)	0.007	0.015
Bond angles (°)	0.8	1.4
Validation		
MolProbity score	1.75	1.94
Clashscore	6.0	8.8
Poor rotamers (%)	0.4	1.0
Ramachandran plot		
Favored (%)	93.59	92.69
Allowed (%)	6.35	7.18
Disallowed (%)	0.06	0.13

692

693

694

695

696 **List of Supplemental Tables (provided as excel files)**

697 **Table S1. Oligo sequences used in this study**

698

699 **Table S2. Source data and summary statistics of cellular viability effect by**
700 **introduction of SARS-CoV-2 viral proteins and mutants**

701

702 **Table S3. Processed Nsp1 mRNA-seq dataset and differential expression analysis**

703 Sup table 3.1 TPM table of Nsp1 mRNA-seq dataset

704 Sup table 3.2 Differential expression Nsp1 vs Vector Control

705 Sup table 3.3 Differential expression Nsp1 Mutant vs Vector Control

706 Sup table 3.4 Differential expression Nsp1 vs Nsp1 Mutant

707

708 **Table S4. DAVID pathway analysis of Nsp1 differentially expressed gene sets**

709 Sup table 4.1 Functional clustering of Nsp1 vs Vector Control highly

710 downregulated genes ($q < 1e-30$)

711 Sup table 4.2 Functional clustering of Nsp1 vs Nsp1 Mutant highly

712 downregulated genes ($q < 1e-30$)

713 Sup table 4.3 Functional clustering of Nsp1 vs Vector Control highly upregulated
714 genes ($q < 1e-30$)

715 Sup table 4.4 Functional clustering of Nsp1 vs Nsp1 Mutant highly upregulated
716 genes ($q < 1e-30$)

717 Sup table 4.5 Biological processes enrichment of Nsp1 vs Vector Control highly
718 downregulated genes ($q < 1e-30$)

719 Sup table 4.6 Biological processes enrichment of Nsp1 vs Nsp1 Mutant highly
720 downregulated genes ($q < 1e-30$)

721 Sup table 4.7 Biological processes enrichment of Nsp1 vs Vector Control highly
722 upregulated genes ($q < 1e-30$)

723 Sup table 4.8 Biological processes enrichment of Nsp1 vs Nsp1 Mutant highly
724 upregulated genes ($q < 1e-30$)

725 Sup table 4.9 Gene list of Nsp1 vs Vector Control highly downregulated genes (q
726 $< 1e-30$)

727 Sup table 4.10 Gene list enrichment of Nsp1 vs Nsp1 Mutant highly
728 downregulated genes ($q < 1e-30$)

729 Sup table 4.11 Gene list enrichment of Nsp1 vs Vector Control highly upregulated
730 genes ($q < 1e-30$)

731 Sup table 4.12 Gene list enrichment of Nsp1 vs Nsp1 Mutant highly upregulated
732 genes ($q < 1e-30$)

733 Sup table 4.13 Gene list of Nsp1 vs Vector Control all downregulated genes ($q <$
734 0.01)

735 Sup table 4.14 Gene list of Nsp1 vs Vector Control all upregulated genes ($q <$
736 0.01)

737

738

739 **STAR Methods.**

740

741 **SARS-CoV-2 plasmid cloning**

742 The cDNA templates of SARS-CoV-2 ORF gene containing plasmids were provided by
743 Dr. Krogan as a gift (Gordon et al., 2020), where the ORFs were primarily cloned into
744 lentiviral expression vector. A non-viral expression vector, pVPSB empty, where ORFs
745 were driven by a constitutive EFS promoter and terminated by a short poly A, was
746 constructed by cloning gBlock fragments (IDT) into pcDNA3.1 vector (Addgene, #52535)
747 by the Gibson assembly (NEB). All ORFs gene encoding fragments were PCR amplified
748 from the lentiviral vectors with ORF-specific forward primers and common reverse
749 primer that containing overlaps that corresponded to flanking sequences of the and
750 KpnI and XhoI restriction sites in the pVPSB empty vector. The primer lists were
751 provided in Table S1. ORFs PCR amplified fragments were gel-purified and cloned into
752 restriction enzyme digested backbone by the Gibson assembly (NEB). A lentiviral vector
753 constitutively expressing a Firefly Luciferase and a puromycin mammalian selection
754 marker (Lenti-Fluc-Puro) was generated by standard molecular cloning. All plasmids
755 were sequenced and harvested by Maxiprep for following assay.

756 **Nsp1 mutant ORF construction**

757 Truncation mutant Nsp1 has triple stop codons introduced after residues 12 (N terminal
758 mutant). Nsp1 mutant3 has R124 and K125 replaced with S124 and E125
759 (R124S/K125E). Nsp1 mutant4 has N128 and K129 were converted to S128 and E129
760 (N128S/K129E). IDT gBlocks were ordered for truncated Nsp1 and different Nsp1
761 mutants with 19~23 bp overlaps that corresponded to flanking sequences of the and
762 AgeI and BstXI restriction sites in the pVPSBA01-Nsp1 plasmid. pVPSBA01-Nsp1

763 plasmid were digested and gel purified, and gBlocks were cloned using the Gibson
764 assembly (NEB).

765 **Generation of stable cell lines**

766 Lentivirus was produced by transfection of co-transgene plasmid (Lenti-Fluc-Puro) and
767 packaging plasmids (psPAX2, pMD2.G) into HEK293FT cells, followed by supernatant
768 harvesting, filtering and concentration with Amicon filters (Sigma). H1299 and Vero E6
769 cells were infected with Lenti-Fluc-Puro lentivirus. After 24 h of virus transduction, cells
770 were selected with 10 µg/mL puromycin, until all cells died in the control group. Luc
771 expressing H1299 and Vero E6 that with puromycin resistance cell lines were obtained
772 and named as H1299-PL and Vero E6-PL (Vero E6-PL for short) respectively.

773 **Mammalian cell culture**

774 H1299, H1299-PL, Vero E6, Vero E6-PL cell lines were cultured in Dulbecco' s
775 modified Eagle' s medium (DMEM; Thermo fisher) supplemented with 10% Fetal
776 bovine serum (FBS, Hyclone), 1% penicillin-streptomycin (Gibco), named as D10
777 medium. Cells were typically passaged every 1-2 days at a split ratio of 1:2 or 1:4 when
778 the confluency reached at 80%.

779 **SARS-CoV-2 ORF mini-screen for cell viability**

780 H1299 cells were plated in white opaque walled microwell assay plates, 25,000 cells per
781 96 well. SARS-CoV-2 ORF plasmids, 1 µg of each, were parallelly transfected with 1 µl
782 lipofectamine 2000, in triplicates. Cell viability was detected at every 24hr after
783 transfection using CellTiter-Glo® Luminescent Cell Viability Assay kit (Promega).
784 Relative viability was normalized to the mean viability of empty vector transfected
785 control group. All procedures followed the manufacturer standard protocol. Luminescent

786 signals were measured by a Plate Reader (PerkinElmer).

787 **Determination of luciferase reporter cell viability**

788 H1299-PL and Vero E6-PL cells were plated in white opaque walled microwell assay
789 plates, 25,000 cells per well in a 96 well. SARS-CoV-2 ORF plasmids, 1 µg of each,
790 were parallelly transfected with 1ul lipofectamine 2000. Cell viability was measured
791 every 24 hr after plasmid transfection by adding 150 µg / ml D-Luciferin (PerkinElmer)
792 using a multi-channel pipette. Luciferase intensity was measured by a Plate Reader
793 (PerkinElmer).

794 **Electroporation with 4D nucleofection**

795 Cells were trypsinized and collected, 1e6 cells were resuspended in SF cell line
796 Nucleofector™ solution with 3 µg plasmid DNA. Cells were transferred into 100 µl
797 Nucleocuvette™ Vessel and NCI-H1299 [H1299] cell specific protocol were utilized
798 according to the manufacturer's protocol (4D-Nucleofector™ X Unit, Lonza). After the
799 pulse application, 100 µl prewarmed D10 medium was added to the electroporated cells
800 in the cuvette. Cells were gently resuspended in the cuvette and transferred into 6 well
801 plate, cultured in incubator. Cells were collected at 24 or 48 hours later for
802 flowcytometry assay and RNA extraction.

803 **Apoptosis flow cytometry assay**

804 Flow cytometry was performed using standard immunology protocols. Briefly,
805 experimental and control cells were electroporated with respective plasmids. After a
806 defined time point, cells were collected, fixed and permeabilized using
807 Fixation/Permeabilization Solution kit (BD). Then antigen-specific antibodies with
808 specific dilutions were added into cells and incubated for 30 min on ice. Cells were

809 washed with cold MACS buffer for 3 times before analyzed on a BD FACSAria
810 cytometer. Antibody used: anti-cleaved Caspase-3(Asp175) (Sigma, 9669s, 1:200).

811 **Gene expression analysis by mRNA sequencing (mRNA-seq, RNA-seq)**

812 For H1299-PL cells electroporated with Nsp1 or Nsp1 mutant, mRNA-seq libraries were
813 prepared following next-generation sequencing (NGS) protocols. Briefly, 1e6 H1299
814 cells were electroporated with 3 µg Nsp1, mutant Nsp1, and relative control plasmids.
815 Electroporation was done in with quadruplicates for each group. Cells were collected
816 24hr post electroporation. Total mRNA was extracted with RNasy Plus Mini Kit (Qiagen).
817 1µg total mRNA each sample was used for the RNA-seq library preparations. A
818 NEBNext® Ultra™ RNA Library Prep Kit for Illumina was employed to perform RNA-seq
819 library preparation and samples were multiplexed using barcoded primers provided by
820 NEBNext® Multiplex Oligos for Illumina® (Index Primers Set 1). All procedures follow
821 the manufacturer standard protocol. Libraries were sequenced with Novaseq system
822 (Illumina).

823 **mRNA-seq data processing, differential expression analysis and pathway** 824 **analysis**

825 The mRNA data processing, transcript quantification, differential expression, and
826 pathway analysis were performed using custom computational programs. In brief, Fastq
827 files from mRNA-seq were used analyzed using the Kallisto quant algorithm for
828 transcript quantification (Bray et al., 2016). Differential expression analysis was
829 performed using Sleuth (Pimentel et al., 2017). Z-scores for time course heatmap were
830 calculated by log2-normalization of gene counts following by scaling by genes.
831 Visualizations of differentially expressed genes such as volcano plots and heatmaps

832 were generated using standard R packages. Differentially upregulated and
833 downregulated genes were subjected to pathway analysis by DAVID (Huang et al., 2007)
834 and/or GSEA (Subramanian et al., 2005). Processed mRNA-seq data, differential
835 expression analysis and pathway analysis results are provided in (Table S3 and S4).

836 **RT-qPCR**

837 Total RNA was extracted from cells using RNasy Plus Mini Kit (Qiagen). Total mRNA
838 was reverse transcribed into cDNA by M-MLV Reverse Transcriptase (Sigma). Samples
839 were collected in triplicates. Gene expression was quantified using Taqman Fast
840 Universal PCR Master Mix (Thermo Fisher) and Taqman probes (Invitrogen). NSP1
841 probe was generated with custom designed according to the Nsp1 DNA sequence in the
842 SARS-CoV-2 genome annotation (2019-nCoV/USA-WA1/2020, accession MN985325).
843 RNA expression level was normalized to *ACTB* (human). Relative mRNA expression
844 was determined via the $\Delta\Delta C_t$ method.

845 **Sample size determination**

846 Sample size was determined according to the lab's prior work or similar approaches in
847 the field.

848 **Replication**

849 All experiments were done with at least three biological replicates. Experimental
850 replications were indicated in detail in methods section and in each figure panel's
851 legend.

852 **Standard statistical analysis**

853 All statistical methods are described in figure legends and/or supplementary Excel
854 tables. The P values and statistical significance were estimated for all analyses. For

855 example, the unpaired, two-sided, T test was used to compare two groups. One-way
856 ANOVA along with multiple comparisons test, was used to compare multiple groups.
857 Multiple-testing correction was done using false discovery rate (FDR) method. Different
858 levels of statistical significance were accessed based on specific p values and type I
859 error cutoffs (0.05, 0.01, 0.001, 0.0001). Data analysis was performed using GraphPad
860 Prism v.8. and/or RStudio.

861 **Ribosome and CrPV IRES purification**

862 40S ribosomal subunits were purified from the rabbit reticulocyte lysate (Green
863 Hectares, USA) as described previously (Lomakin and Steitz, 2013). The gene for wild-
864 type CrPV IRES (nucleotides 6028-6240) was chemically synthesized and cloned in the
865 pBluescript SK vector flanked at the 5'-end by a T7 promoter sequence and an EcoRI
866 cleavage site at the 3'-end. Standard *in vitro* transcription protocol was used for IRES
867 RNA synthesis and purification (MEGAscript™ T7 Transcription Kit, Ambion, USA).

868 **Protein construction, expression and purification**

869 Full-length SARS-CoV-2 Nsp1 was cloned into pMAT-9s vector and pET-Duet vector for
870 expression of MBP-tagged and 6xhis tagged proteins, respectively. The Escherichia coli
871 BL21 (DE3) cells were used for protein expressions, which were induced by 0.5 mM
872 isopropyl β -D-1-thiogalactopyranoside (IPTG) at 16 °C for 16 hours in Terrific Broth.
873 Cells were harvested and lysed using a microfluidizer. The lysate was clarified by
874 centrifugation and then applied to a Ni-NTA (Qiagen) column. Anion exchange (HiTrap
875 Q HP, GE healthcare) chromatography was performed in a buffer of 50 mM Tris, pH 8.0
876 with a NaCl concentration gradient from 50 mM to 1M. Subsequent size exclusion
877 chromatography (HiLoad Superdex 75, GE healthcare) was performed in a buffer of 50

878 mM Tris, 150 mM NaCl, pH 8.0. Purity of the proteins was analyzed by SDS-PAGE after
879 each step. Full length eIF3j was expressed in Escherichia coli BL21 and purified with a
880 similar method.

881 **Filter binding assays**

882 Rabbit 40S ribosome and binding partners (proteins or CrPV IRES RNA) were
883 incubated together for 20 min at 37 °C in a total volume of 20 µl in 1× 48S buffer (20
884 mM HEPES(KOH) pH 7.5, 100 mM KCl, 2.5 mM MgAc, 1 mM DTT, 250 µM Spermidine
885 3HCl). Reaction mixtures were incubated for another 20 min at room temperature
886 before diluting to 100 µl with H100 buffer (10 mM HEPES(KOH) pH 7.0, 100 mM KCl, 5
887 mM MgAc, 2 mM DTT). Diluted reaction mixtures were filtered through 100 kDa filter
888 (Thermo Scientific) in 10,000g for 5 min. The flow through was collected. 200 µl H100
889 buffer was used for washing the unbound proteins or RNA for 4 times before analyzing
890 by SDS-PAGE or RNA gel.

891 The concentration for the 40S ribosome for the filter binding assay is 1.5 µM and
892 the Nsp1 concentration is 15 µM (ratio of 1:10). In the Nsp1 and eIF3j competition
893 assays, the concentrations of eIF3j are 7.5 µM, 15 µM and 30 µM corresponding to
894 ratios of 1:5, 1:10 and 1:20. The concentration of the CrPV IRES is 7.5 µM in the Nsp1-
895 IRES binding assay (ratio of 1:5).

896 **Cryo-EM sample preparation, data collection and processing**

897 40S ribosome and Nsp1, with or without the CrPV IRES RNA were mixed and incubated
898 at 37 °C for 20 mins to form a stable complex. The complex (4 µl) was applied to a C-
899 Flat 2/1 3C copper grid (Electron Microscopy Sciences) pretreated by glow-discharging
900 at 8 mA for 20 seconds. The grid was blotted at 20 °C with 100% humidity and plunge-

901 frozen in liquid ethane using FEI Vitrobot Mark IV (Thermo Fisher). The grids were
902 stored in liquid nitrogen before data collection.

903 Images were acquired on a FEI Titan Krios electron microscope (Thermo Fisher)
904 equipped with a post-GIF Gatan K3 direct detector in super-resolution mode, at a
905 nominal calibrated magnification of 81,000x with the physical pixel size corresponding
906 to 1.068Å. Automated data collection was performed using SerialEM (Mastronarde,
907 2005).

908 A total of 4,700 movie series were collected for the Nsp1-40S ribosome complex.
909 300 movies series were collected for the Nsp1-40S-CrPV IRES complex. For the Nsp1-
910 40S ribosome complex, a defocus range of 0.5 µm to 2 µm was used. Data were
911 collected with a dose of 15.9 electrons per pixel per second. Images were recorded over
912 a 3.6s exposure with 0.1s for each frame to give a total dose of 50 electrons per Å².
913 Similar conditions were used for the Nsp1-40S-CrPV IRES complex.

914 The same data processing procedures were carried out for both the two
915 complexes using standard pipelines in cryoSPARC(Punjani et al., 2017). The final
916 average resolution is 2.7 Å for the Nsp1-40S ribosome complex and 3.3 Å for the Nsp1-
917 40S-CrPV IRES complex (FSC=0.143). Local refinement was carried out for the head
918 domain of the 40S, which significantly increased the quality of the reconstruction for this
919 domain (Figure S4C).

920 **Model building and refinement**

921 The structure of the rabbit 40S ribosome was extracted from PDB: 4KZX (Lomakin and
922 Steitz, 2013) and 6SGC (Chandrasekaran et al., 2019). The model of Nsp1 C-terminal
923 domain was manually built in COOT (Emsley et al., 2010). The CrPV IRES structure

924 was extracted from PDB:5IT9 and refined (Murray et al., 2016). The structures of Nsp1-
925 40S ribosome complex and Nsp1-IRES-40S ribosome complex were refined with
926 phenix.real_space_refine module in PHENIX (Adams et al., 2010). All structural figures
927 were generated using PyMol (Schrodinger, 2015) and Chimera (Pettersen et al., 2004).

928

929 **Data and resource availability**

930 All data generated or analyzed during this study are included in this article and its
931 supplementary information files. Specifically, source data and statistics for non-high-
932 throughput experiments are provided in a supplementary table excel file (Table S2).
933 High-throughput experiment data are provided as processed quantifications in
934 Supplemental Datasets (Table S3 and S4). Genomic sequencing raw data are being
935 deposited to NIH Sequence Read Archive (SRA) and/or Gene Expression Omnibus
936 (GEO), with pending accession numbers. Constructs are available at either through a
937 public repository or via requests to the corresponding authors. Original cell lines are
938 available at commercial sources listed in supplementary information files. Genetically
939 modified cell lines are available via the authors' laboratories. Codes that support the
940 findings of this research are being deposited to a public repository such as GitHub, and
941 are available from the corresponding authors upon reasonable request.

942 The cryo-EM maps of the Nsp1-40S ribosome complex and the Nsp1-40S-CrPV
943 IRES ribosome complex have been deposited in the Electron Microscopy Data Bank as
944 EMD-XXXX and EMD-YYYY, respectively. The corresponding structure models are in
945 the Protein Data Bank with accession code XXXX, YYYY.

946

947 **References:**

- 948 Adams, P.D., Afonine, P.V., Bunkoczi, G., Chen, V.B., Davis, I.W., Echols, N., Headd, J.J., Hung, L.W., Kapral, G.J.,
949 Grosse-Kunstleve, R.W., *et al.* (2010). PHENIX: a comprehensive Python-based system for macromolecular structure
950 solution. *Acta Crystallogr D Biol Crystallogr* *66*, 213-221.
- 951 Almeida, M.S., Johnson, M.A., Herrmann, T., Geralt, M., and Wuthrich, K. (2007). Novel beta-barrel fold in the
952 nuclear magnetic resonance structure of the replicase nonstructural protein 1 from the severe acute respiratory
953 syndrome coronavirus. *J Virol* *81*, 3151-3161.
- 954 Astuti, I., and Ysrafil (2020). Severe Acute Respiratory Syndrome Coronavirus 2 (SARS-CoV-2): An overview of viral
955 structure and host response. *Diabetes Metab Syndr* *14*, 407-412.
- 956 Aylett, C.H., Boehringer, D., Erzberger, J.P., Schaefer, T., and Ban, N. (2015). Structure of a yeast 40S-eIF1-eIF1A-eIF3-
957 eIF3j initiation complex. *Nat Struct Mol Biol* *22*, 269-271.
- 958 Babaylova, E., Malygin, A., Gopanenko, A., Graifer, D., and Karpova, G. (2019a). Tetrapeptide 60-63 of human
959 ribosomal protein uS3 is crucial for translation initiation. *Biochim Biophys Acta Gene Regul Mech* *1862*, 194411.
- 960 Babaylova, E., Malygin, A., Gopanenko, A., Graifer, D., and Karpova, G. (2019b). Tetrapeptide 60-63 of human
961 ribosomal protein uS3 is crucial for translation initiation. *Bba-Gene Regul Mech* *1862*.
- 962 Blanco-Melo, D., Nilsson-Payant, B.E., Liu, W.C., Uhl, S., Hoagland, D., Moller, R., Jordan, T.X., Oishi, K., Panis, M.,
963 Sachs, D., *et al.* (2020). Imbalanced Host Response to SARS-CoV-2 Drives Development of COVID-19. *Cell* *181*, 1036-
964 1045 e1039.
- 965 Bray, N.L., Pimentel, H., Melsted, P., and Pachter, L. (2016). Near-optimal probabilistic RNA-seq quantification. *Nat*
966 *Biotechnol* *34*, 525-527.
- 967 Cate, J.H. (2017). Human eIF3: from 'blobology' to biological insight. *Philos Trans R Soc Lond B Biol Sci* *372*.
- 968 Chandrasekaran, V., Juszkiewicz, S., Choi, J., Puglisi, J.D., Brown, A., Shao, S., Ramakrishnan, V., and Hegde, R.S.
969 (2019). Mechanism of ribosome stalling during translation of a poly(A) tail. *Nat Struct Mol Biol* *26*, 1132-1140.
- 970 Coronaviridae Study Group of the International Committee on Taxonomy of, V. (2020). The species Severe acute
971 respiratory syndrome-related coronavirus: classifying 2019-nCoV and naming it SARS-CoV-2. *Nat Microbiol* *5*, 536-
972 544.
- 973 Dong, J.S., Aitken, C.E., Thakur, A., Shin, B.S., Lorsch, J.R., and Hinnebusch, A.G. (2017). Rps3/uS3 promotes mRNA
974 binding at the 40S ribosome entry channel and stabilizes preinitiation complexes at start codons. *P Natl Acad Sci*
975 *USA* *114*, E2126-E2135.
- 976 Emsley, P., Lohkamp, B., Scott, W.G., and Cowtan, K. (2010). Features and development of Coot. *Acta Crystallogr D*
977 *Biol Crystallogr* *66*, 486-501.
- 978 Fraser, C.S., Berry, K.E., Hershey, J.W.B., and Doudna, J.A. (2007). eIF3j is located in the decoding center of the
979 human 40S ribosomal subunit. *Mol Cell* *26*, 811-819.
- 980 Fraser, C.S., Lee, J.Y., Mayeur, G.L., Bushell, M., Doudna, J.A., and Hershey, J.W. (2004a). The j-subunit of human
981 translation initiation factor eIF3 is required for the stable binding of eIF3 and its subcomplexes to 40 S ribosomal
982 subunits in vitro. *J Biol Chem* *279*, 8946-8956.
- 983 Fraser, C.S., Lee, J.Y., Mayeur, G.L., Bushell, M., Doudna, J.A., and Hershey, J.W.B. (2004b). The j-subunit of human
984 translation initiation factor eIF3 is required for the stable binding of eIF3 and its subcomplexes to 40 S ribosomal
985 subunits in vitro. *J Biol Chem* *279*, 8946-8956.
- 986 Gordon, D.E., Jang, G.M., Bouhaddou, M., Xu, J., Obernier, K., White, K.M., O'Meara, M.J., Rezelj, V.V., Guo, J.Z.,
987 Swaney, D.L., *et al.* (2020). A SARS-CoV-2 protein interaction map reveals targets for drug repurposing. *Nature* *583*,
988 459-468.
- 989 Graifer, D., Malygin, A., Zharkov, D.O., and Karpova, G. (2014). Eukaryotic ribosomal protein S3: A constituent of
990 translational machinery and an extraribosomal player in various cellular processes. *Biochimie* *99*, 8-18.
- 991 Grasselli, G., Zangrillo, A., Zanella, A., Antonelli, M., Cabrini, L., Castelli, A., Cereda, D., Coluccello, A., Foti, G.,
992 Fumagalli, R., *et al.* (2020). Baseline Characteristics and Outcomes of 1591 Patients Infected With SARS-CoV-2
993 Admitted to ICUs of the Lombardy Region, Italy. *JAMA*.
- 994 Haimov, O., Sinvani, H., Martin, F., Ulitsky, I., Emmanuel, R., Tamarkin-Ben-Harush, A., Vardy, A., and Dikstein, R.
995 (2017). Efficient and Accurate Translation Initiation Directed by TISU Involves RPS3 and RPS10e Binding and
996 Differential Eukaryotic Initiation Factor 1A Regulation. *Mol Cell Biol* *37*.
- 997 Hashem, Y., des Georges, A., Dhote, V., Langlois, R., Liao, H.Y., Grassucci, R.A., Pestova, T.V., Hellen, C.U., and Frank, J.

998 (2013). Hepatitis-C-virus-like internal ribosome entry sites displace eIF3 to gain access to the 40S subunit. *Nature*
999 *503*, 539-543.

1000 Hershey, J.W. (2015). The role of eIF3 and its individual subunits in cancer. *Biochim Biophys Acta* *1849*, 792-800.

1001 Hinnebusch, A.G. (2014). The scanning mechanism of eukaryotic translation initiation. *Annu Rev Biochem* *83*, 779-
1002 812.

1003 Hinnebusch, A.G. (2017a). Structural Insights into the Mechanism of Scanning and Start Codon Recognition in
1004 Eukaryotic Translation Initiation. *Trends Biochem Sci* *42*, 589-611.

1005 Hinnebusch, A.G. (2017b). Structural Insights into the Mechanism of Scanning and Start Codon Recognition in
1006 Eukaryotic Translation Initiation. *Trends Biochem Sci* *42*, 589-611.

1007 Hinnebusch, A.G., Ivanov, I.P., and Sonenberg, N. (2016). Translational control by 5'-untranslated regions of
1008 eukaryotic mRNAs. *Science* *352*, 1413-1416.

1009 Hoffmann, M., Kleine-Weber, H., Schroeder, S., Kruger, N., Herrler, T., Erichsen, S., Schiergens, T.S., Herrler, G., Wu,
1010 N.H., Nitsche, A., *et al.* (2020). SARS-CoV-2 Cell Entry Depends on ACE2 and TMPRSS2 and Is Blocked by a Clinically
1011 Proven Protease Inhibitor. *Cell* *181*, 271-+.

1012 Huang, C., Lokugamage, K.G., Rozovics, J.M., Narayanan, K., Semler, B.L., and Makino, S. (2011). SARS coronavirus
1013 nsp1 protein induces template-dependent endonucleolytic cleavage of mRNAs: viral mRNAs are resistant to nsp1-
1014 induced RNA cleavage. *Plos Pathog* *7*, e1002433.

1015 Huang, D.W., Sherman, B.T., Tan, Q., Collins, J.R., Alvord, W.G., Roayaei, J., Stephens, R., Baseler, M.W., Lane, H.C.,
1016 and Lempicki, R.A. (2007). The DAVID Gene Functional Classification Tool: a novel biological module-centric
1017 algorithm to functionally analyze large gene lists. *Genome Biol* *8*, R183.

1018 Jan, E., Mohr, I., and Walsh, D. (2016). A Cap-to-Tail Guide to mRNA Translation Strategies in Virus-Infected Cells.
1019 *Annu Rev Virol* *3*, 283-307.

1020 Kamitani, W., Huang, C., Narayanan, K., Lokugamage, K.G., and Makino, S. (2009). A two-pronged strategy to
1021 suppress host protein synthesis by SARS coronavirus Nsp1 protein. *Nat Struct Mol Biol* *16*, 1134-U1132.

1022 Kamitani, W., Narayanan, K., Huang, C., Lokugamage, K., Ikegami, T., Ito, N., Kubo, H., and Makino, S. (2006). Severe
1023 acute respiratory syndrome coronavirus nsp1 protein suppresses host gene expression by promoting host mRNA
1024 degradation. *Proc Natl Acad Sci U S A* *103*, 12885-12890.

1025 Kim, D., Lee, J.Y., Yang, J.S., Kim, J.W., Kim, V.N., and Chang, H. (2020). The Architecture of SARS-CoV-2
1026 Transcriptome. *Cell* *181*, 914-921 e910.

1027 Lee, A.S., Kranzusch, P.J., Doudna, J.A., and Cate, J.H. (2016). eIF3d is an mRNA cap-binding protein that is required
1028 for specialized translation initiation. *Nature* *536*, 96-99.

1029 Lim, Y.X., Ng, Y.L., Tam, J.P., and Liu, D.X. (2016). Human Coronaviruses: A Review of Virus-Host Interactions.
1030 *Diseases* *4*.

1031 Lokugamage, K.G., Narayanan, K., Huang, C., and Makino, S. (2012). Severe Acute Respiratory Syndrome
1032 Coronavirus Protein nsp1 Is a Novel Eukaryotic Translation Inhibitor That Represses Multiple Steps of Translation
1033 Initiation. *J Virol* *86*, 13598-13608.

1034 Lomakin, I.B., and Steitz, T.A. (2013). The initiation of mammalian protein synthesis and mRNA scanning
1035 mechanism. *Nature* *500*, 307-311.

1036 Lozano, G., and Martinez-Salas, E. (2015). Structural insights into viral IRES-dependent translation mechanisms.
1037 *Curr Opin Virol* *12*, 113-120.

1038 Martinez-Salas, E., Francisco-Velilla, R., Fernandez-Chamorro, J., and Embarek, A.M. (2018). Insights into Structural
1039 and Mechanistic Features of Viral IRES Elements. *Front Microbiol* *8*.

1040 Masters, P.S. (2006). The molecular biology of coronaviruses. *Adv Virus Res* *66*, 193-292.

1041 Mastrorarde, D.N. (2005). Automated electron microscope tomography using robust prediction of specimen
1042 movements. *J Struct Biol* *152*, 36-51.

1043 Murray, J., Savva, C.G., Shin, B.S., Dever, T.E., Ramakrishnan, V., and Fernandez, I.S. (2016). Structural
1044 characterization of ribosome recruitment and translocation by type IV IRES. *Elife* *5*.

1045 Narayanan, K., Huang, C., Lokugamage, K., Kamitani, W., Ikegami, T., Tseng, C.T., and Makino, S. (2008). Severe acute
1046 respiratory syndrome coronavirus nsp1 suppresses host gene expression, including that of type I interferon, in
1047 infected cells. *J Virol* *82*, 4471-4479.

1048 Niepmann, M., and Gerresheim, G.K. (2020). Hepatitis C Virus Translation Regulation. *Int J Mol Sci* *21*.

1049 Passmore, L.A., Schmeing, T.M., Maag, D., Applefield, D.J., Acker, M.G., Algire, M.A., Lorsch, J.R., and Ramakrishnan,
1050 V. (2007). The eukaryotic translation initiation factors eIF1 and eIF1A induce an open conformation of the 40S

1051 ribosome. *Mol Cell* 26, 41-50.

1052 Pettersen, E.F., Goddard, T.D., Huang, C.C., Couch, G.S., Greenblatt, D.M., Meng, E.C., and Ferrin, T.E. (2004). UCSF

1053 Chimera--a visualization system for exploratory research and analysis. *J Comput Chem* 25, 1605-1612.

1054 Pimentel, H., Bray, N.L., Puente, S., Melsted, P., and Pachter, L. (2017). Differential analysis of RNA-seq incorporating

1055 quantification uncertainty. *Nat Methods* 14, 687-690.

1056 Pisarev, A.V., Kolupaeva, V.G., Yusupov, M.M., Hellen, C.U., and Pestova, T.V. (2008). Ribosomal position and

1057 contacts of mRNA in eukaryotic translation initiation complexes. *The EMBO journal* 27, 1609-1621.

1058 Punjani, A., Rubinstein, J.L., Fleet, D.J., and Brubaker, M.A. (2017). cryoSPARC: algorithms for rapid unsupervised

1059 cryo-EM structure determination. *Nat Methods* 14, 290-296.

1060 Schrodinger, LLC (2015). The PyMOL Molecular Graphics System, Version 1.8.

1061 Sharifulin, D.E., Bartuli, Y.S., Meschaninova, M.I., Ven'yaminova, A.G., Graifer, D.M., and Karpova, G.G. (2016).

1062 Exploring accessibility of structural elements of the mammalian 40S ribosomal mRNA entry channel at various

1063 steps of translation initiation. *Bba-Proteins Proteom* 1864, 1328-1338.

1064 Sharifulin, D.E., Grosheva, A.S., Bartuli, Y.S., Malygin, A.A., Meschaninova, M.I., Ven'yaminova, A.G., Stahl, J., Graifer,

1065 D.M., and Karpova, G.G. (2015). Molecular contacts of ribose-phosphate backbone of mRNA with human ribosome.

1066 *Bba-Gene Regul Mech* 1849, 930-939.

1067 Sokabe, M., and Fraser, C.S. (2014). Human eukaryotic initiation factor 2 (eIF2)-GTP-Met-tRNAi ternary complex

1068 and eIF3 stabilize the 43 S preinitiation complex. *J Biol Chem* 289, 31827-31836.

1069 Subramanian, A., Tamayo, P., Mootha, V.K., Mukherjee, S., Ebert, B.L., Gillette, M.A., Paulovich, A., Pomeroy, S.L.,

1070 Golub, T.R., Lander, E.S., *et al.* (2005). Gene set enrichment analysis: a knowledge-based approach for interpreting

1071 genome-wide expression profiles. *Proc Natl Acad Sci U S A* 102, 15545-15550.

1072 Tanaka, T., Kamitani, W., DeDiego, M.L., Enjuanes, L., and Matsuura, Y. (2012). Severe acute respiratory syndrome

1073 coronavirus nsp1 facilitates efficient propagation in cells through a specific translational shutoff of host mRNA. *J*

1074 *Viro* 86, 11128-11137.

1075 Thoms, M., Buschauer, R., Ameisemeier, M., Koepke, L., Denk, T., Hirschenberger, M., Kratzat, H., Hayn, M., Mackens-

1076 Kiani, T., Cheng, J., *et al.* (2020). Structural basis for translational shutdown and immune evasion by the Nsp1

1077 protein of SARS-CoV-2. *Science*.

1078 Tohya, Y., Narayanan, K., Kamitani, W., Huang, C., Lokugamage, K., and Makino, S. (2009). Suppression of host gene

1079 expression by nsp1 proteins of group 2 bat coronaviruses. *J Virol* 83, 5282-5288.

1080 Walker, M.J., Shortridge, M.D., Albin, D.D., Cominsky, L.Y., and Varani, G. (2020). Structure of the RNA Specialized

1081 Translation Initiation Element that Recruits eIF3 to the 5'-UTR of c-Jun. *J Mol Biol* 432, 1841-1855.

1082 Walsh, D., and Mohr, I. (2011). Viral subversion of the host protein synthesis machinery. *Nat Rev Microbiol* 9, 860-

1083 875.

1084 Wathelet, M.G., Orr, M., Frieman, M.B., and Baric, R.S. (2007). Severe acute respiratory syndrome coronavirus

1085 evades antiviral signaling: role of nsp1 and rational design of an attenuated strain. *J Virol* 81, 11620-11633.

1086 Wei, J., Alfajaro, M.M., Hanna, R.E., DeWeirdt, P.C., Strine, M.S., Lu-Culligan, W.J., Zhang, S.-M., Graziano, V.R.,

1087 Schmitz, C.O., Chen, J.S., *et al.* (2020). Genome-wide CRISPR screen reveals host genes that regulate SARS-CoV-2

1088 infection. *bioRxiv*, 2020.2006.2016.155101.

1089 Wong, H.H., Kumar, P., Tay, F.P.L., Moreau, D., Liu, D.X., and Bard, F. (2015). Genome-Wide Screen Reveals Valosin-

1090 Containing Protein Requirement for Coronavirus Exit from Endosomes. *J Virol* 89, 11116-11128.

1091 Yoshimoto, F.K. (2020). The Proteins of Severe Acute Respiratory Syndrome Coronavirus-2 (SARS CoV-2 or n-COV19),

1092 the Cause of COVID-19. *Protein J* 39, 198-216.

1093 Zhou, P., Yang, X.L., Wang, X.G., Hu, B., Zhang, L., Zhang, W., Si, H.R., Zhu, Y., Li, B., Huang, C.L., *et al.* (2020). A

1094 pneumonia outbreak associated with a new coronavirus of probable bat origin. *Nature* 579, 270-273.

1095 Ziebuhr, J. (2005). The coronavirus replicase. *Curr Top Microbiol Immunol* 287, 57-94.

1096 Züst, R., Cervantes-Barragan, L., Kuri, T., Blakqori, G., Weber, F., Ludewig, B., and Thiel, V. (2007). Coronavirus non-

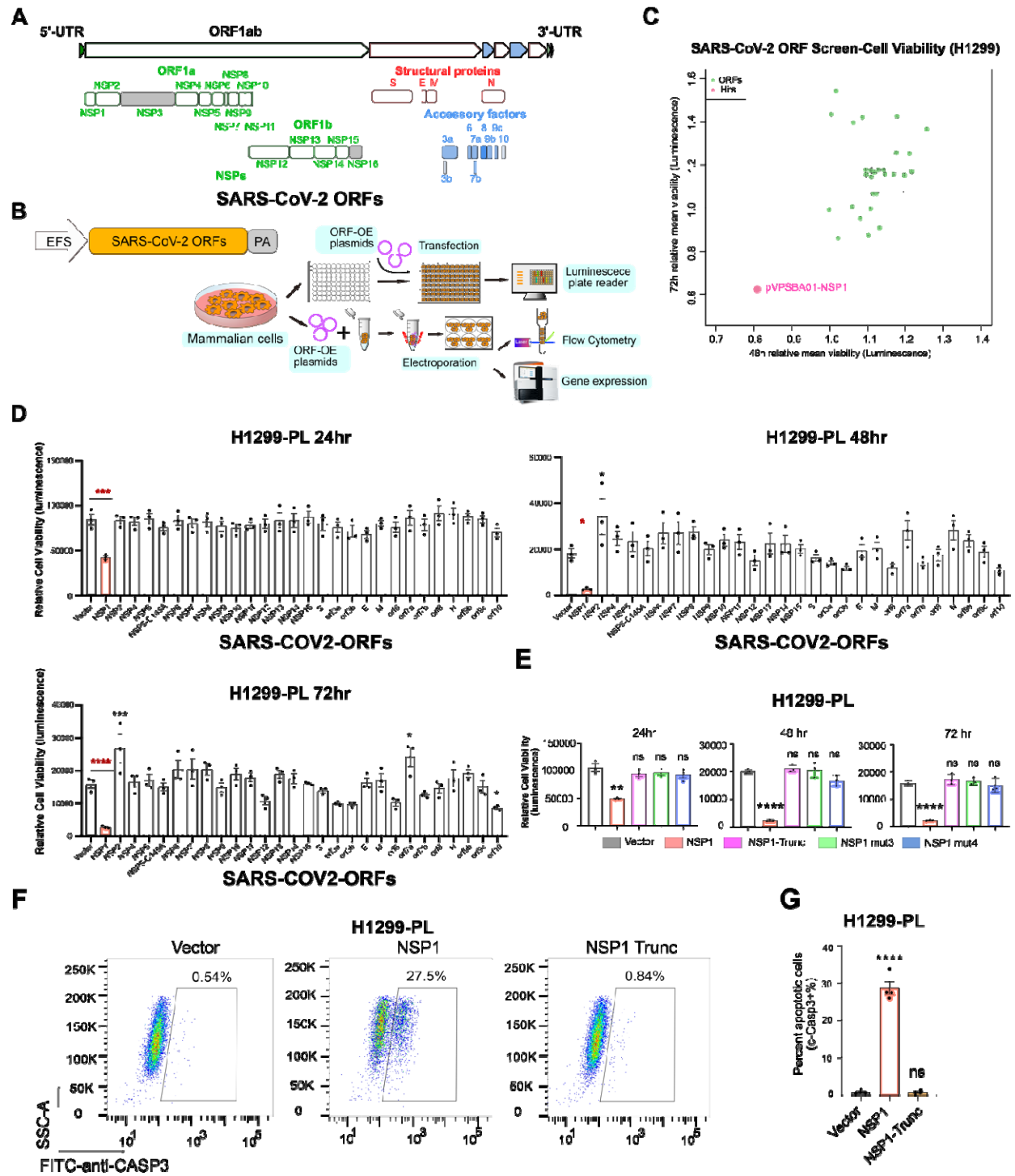
1097 structural protein 1 is a major pathogenicity factor: Implications for the rational design of coronavirus vaccines. *Plos*

1098 *Pathog* 3, 1062-1072.

1099

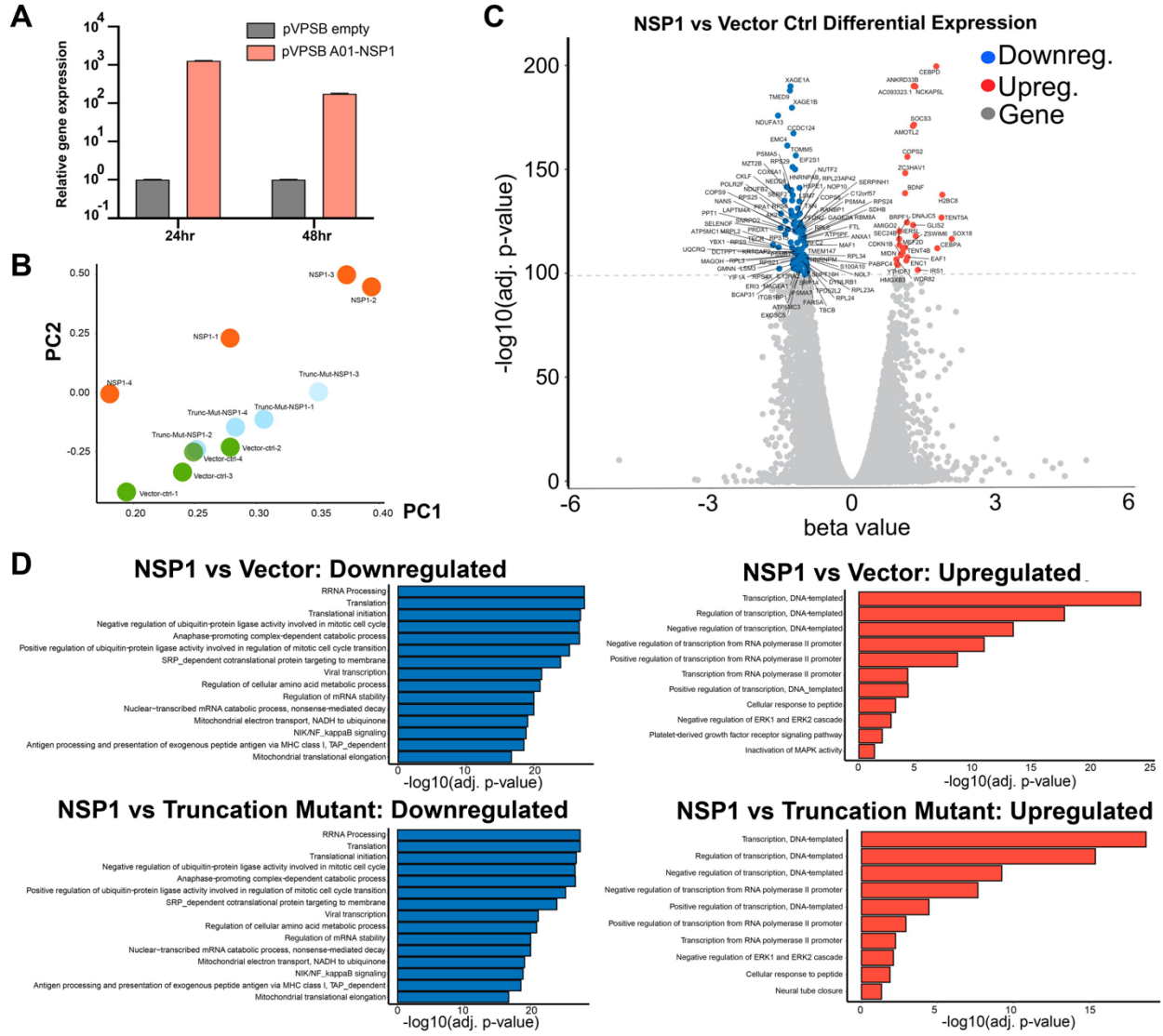
1100

Figure 1



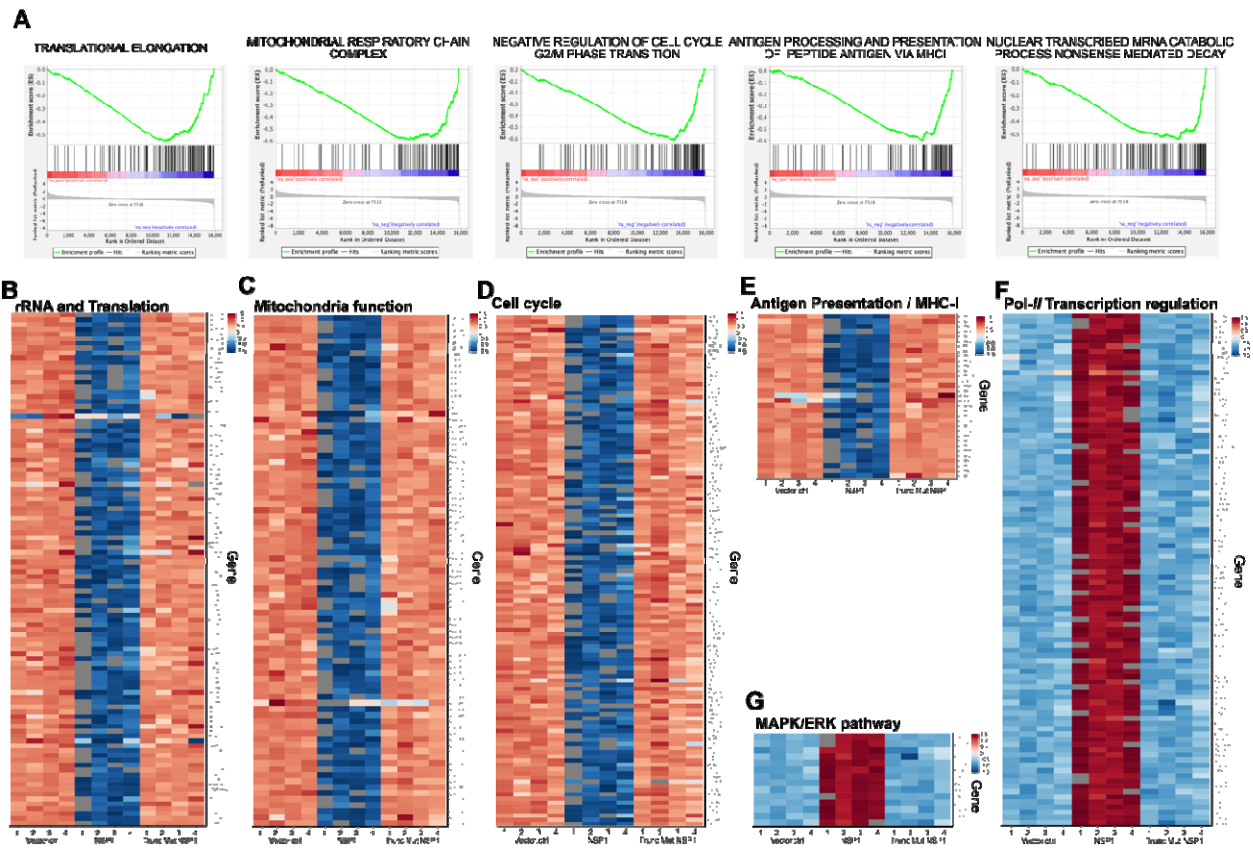
1101

Figure 2



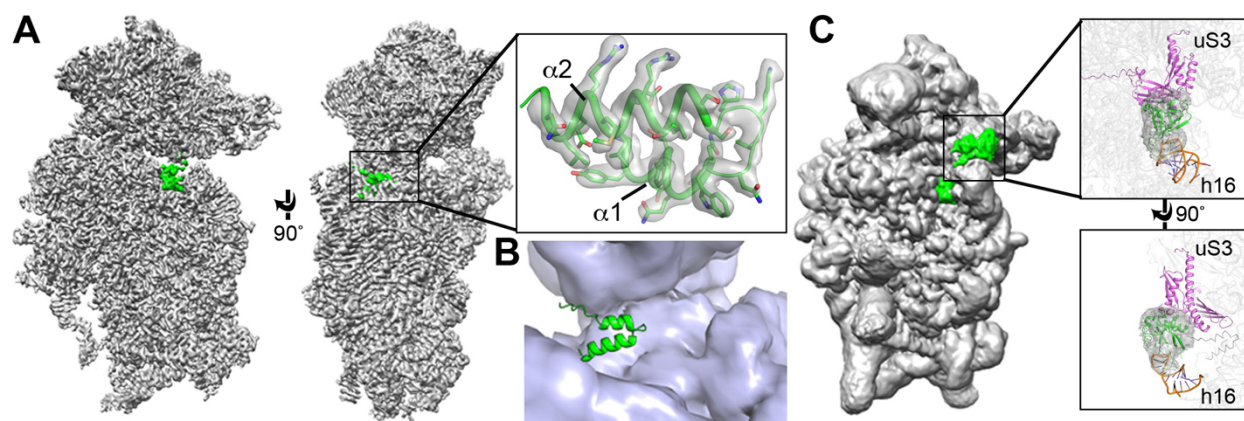
1102

Figure 3



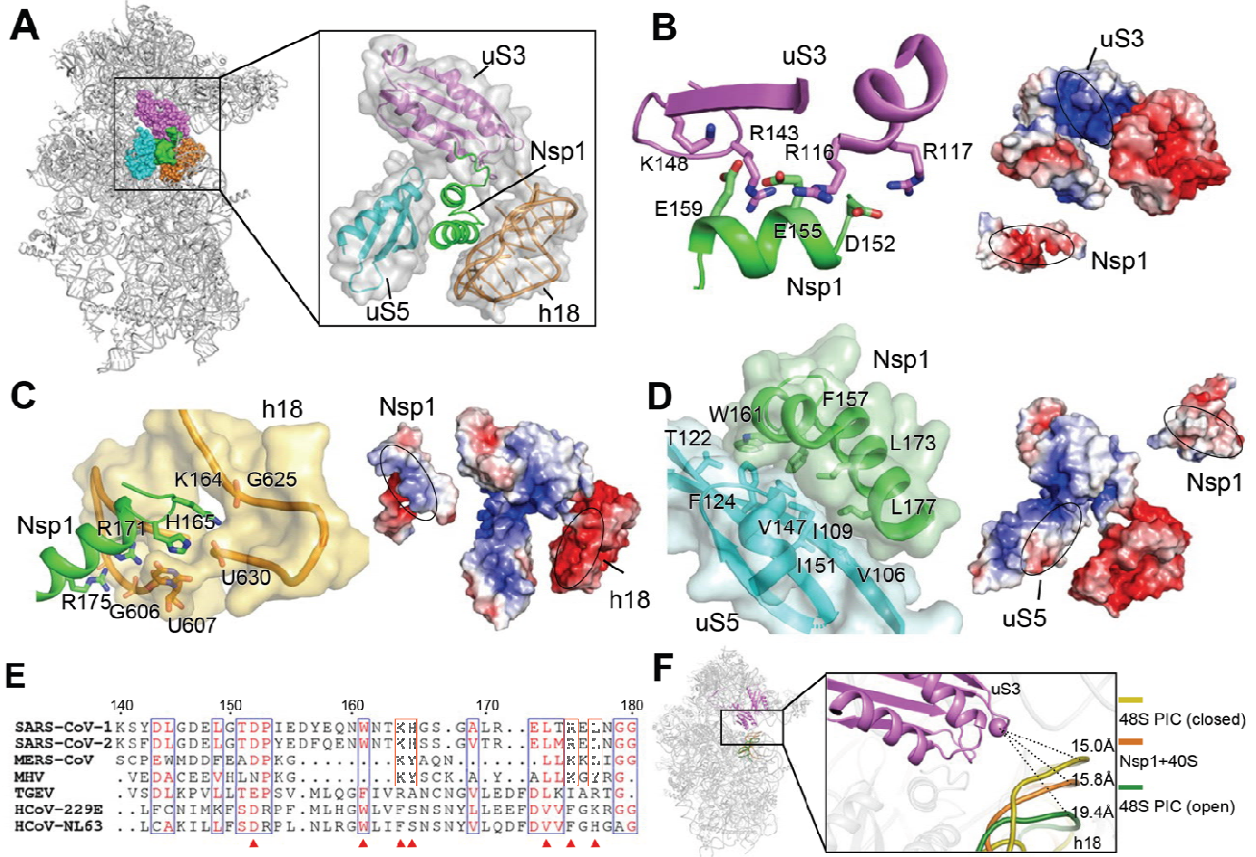
1103
1104

Figure 4



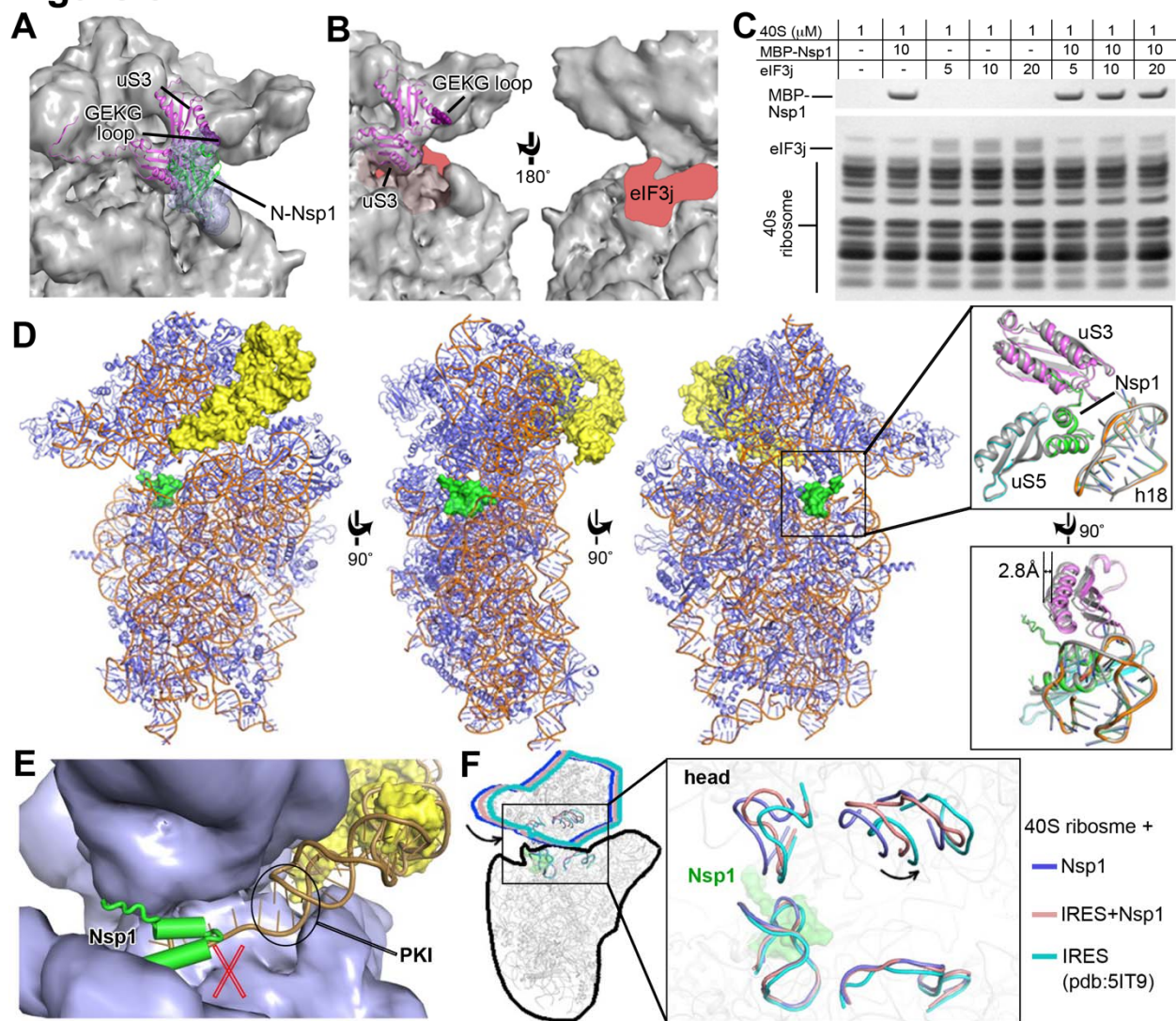
1105
1106

Figure 5



1107

Figure 6



1108

Figure S1

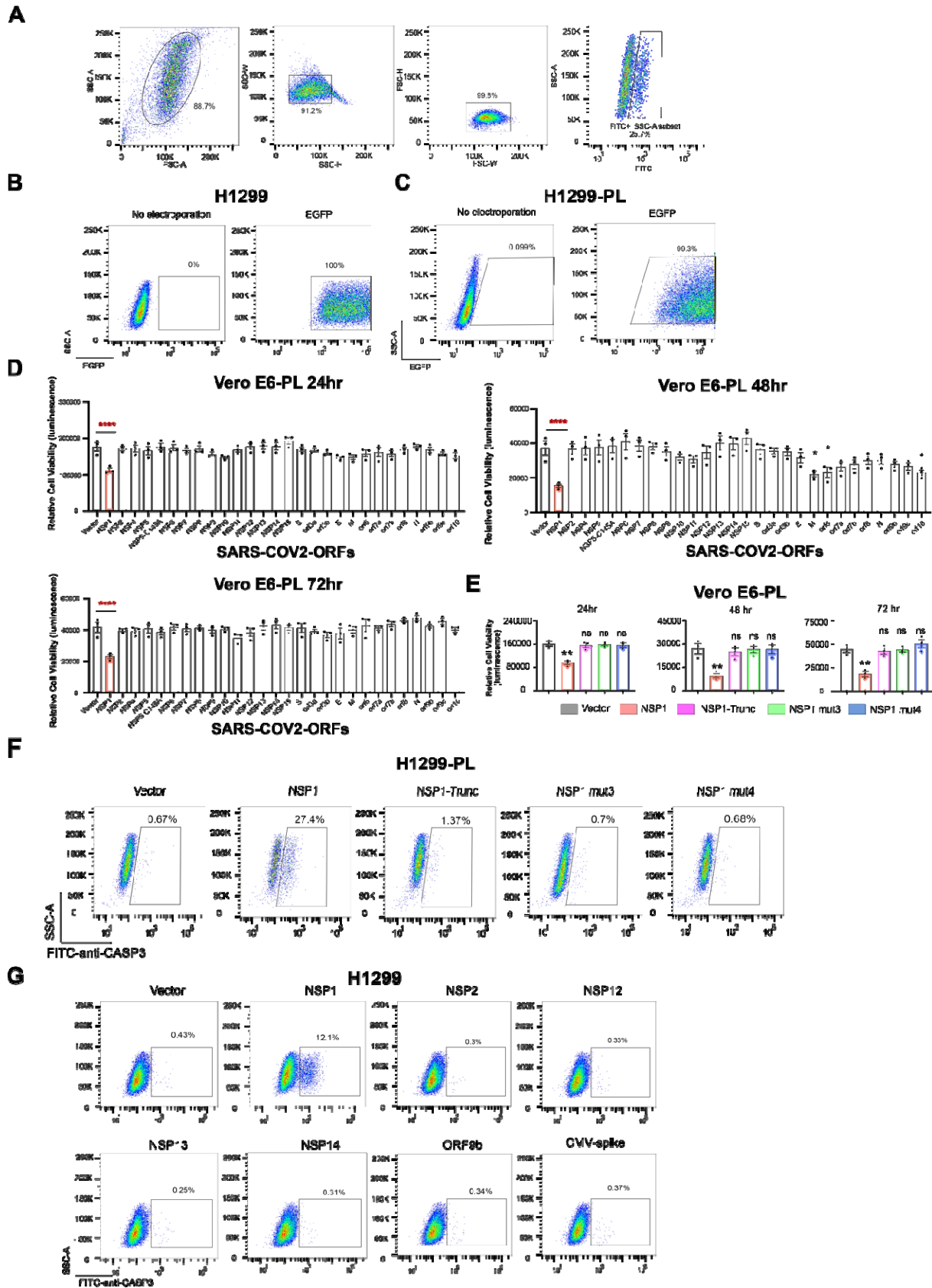


Figure S2

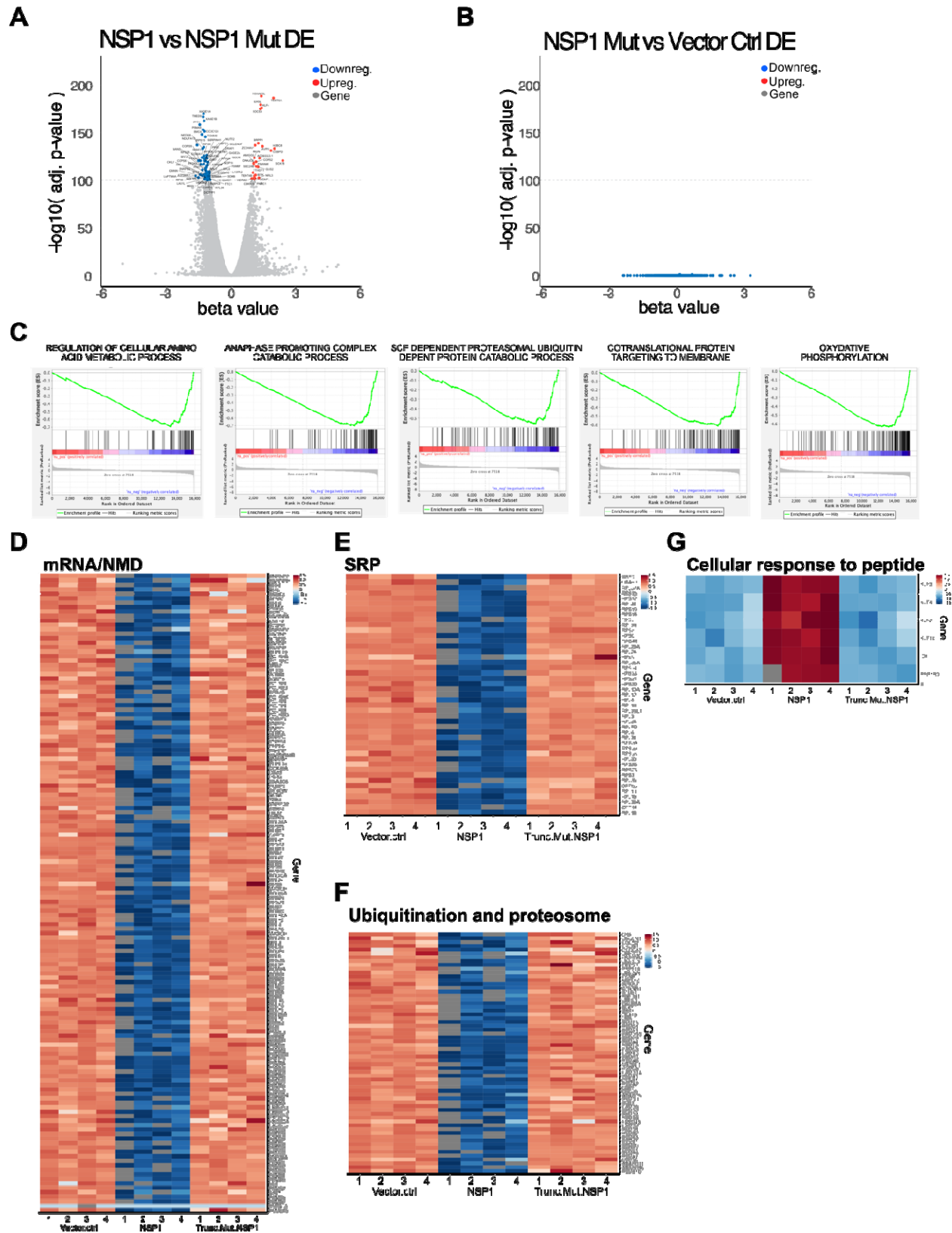
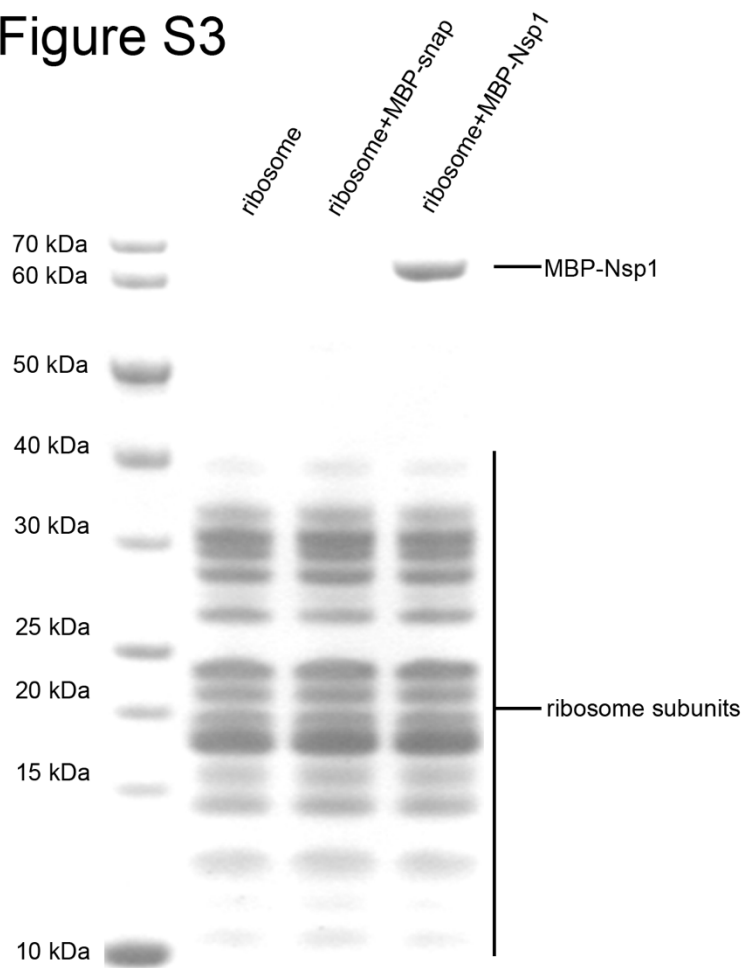


Figure S3



1111

Figure S4

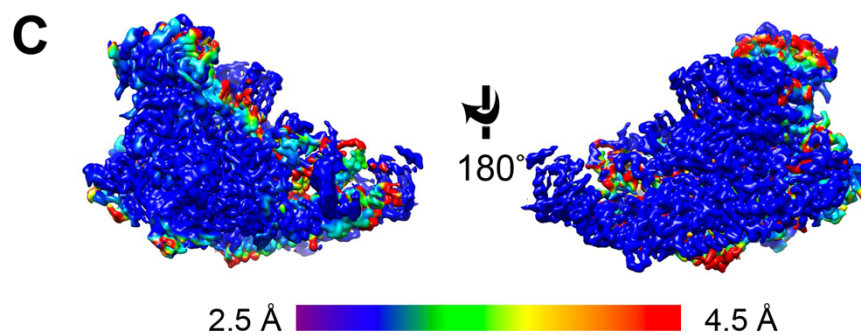
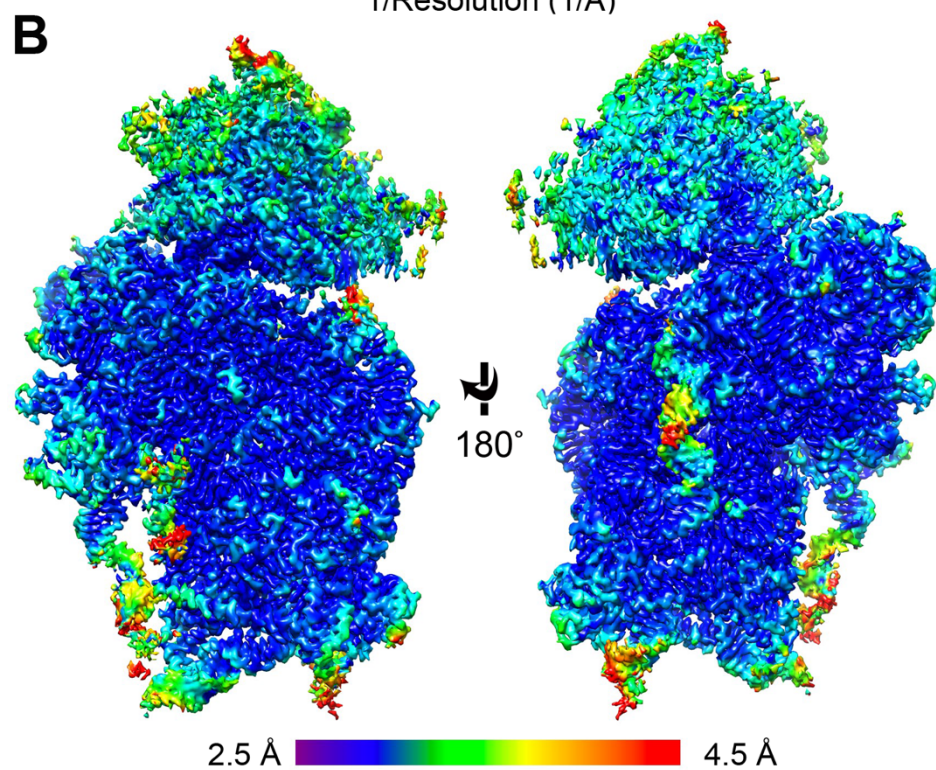
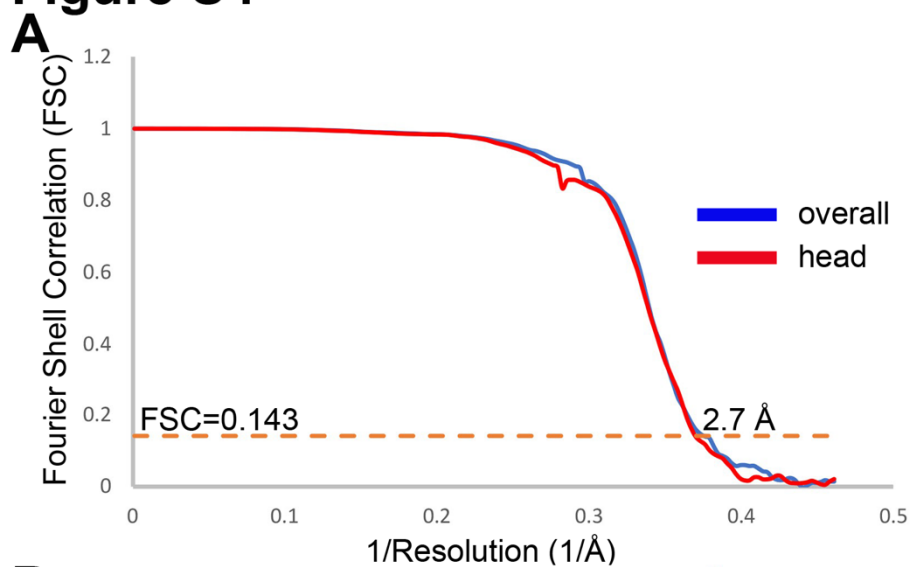
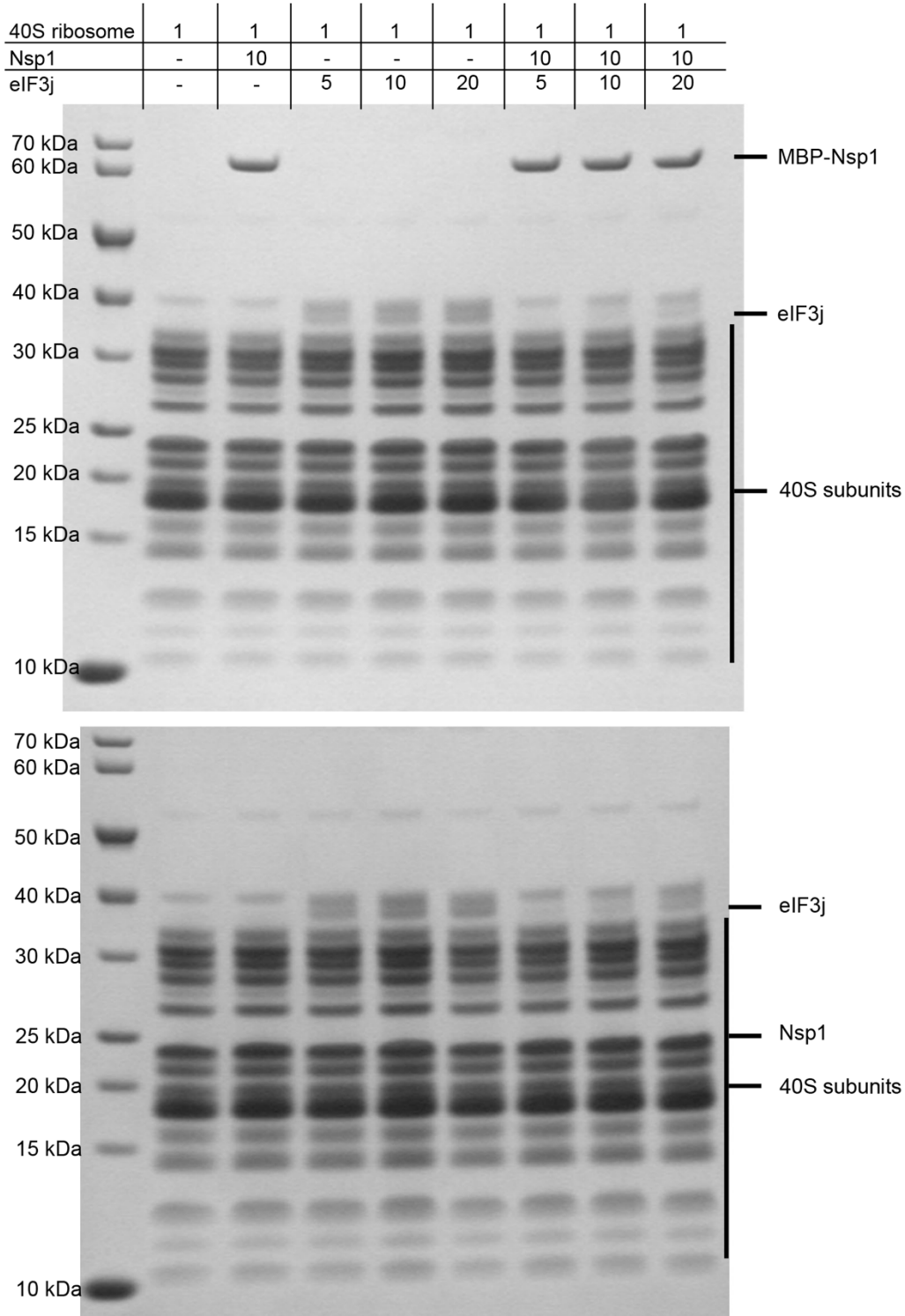
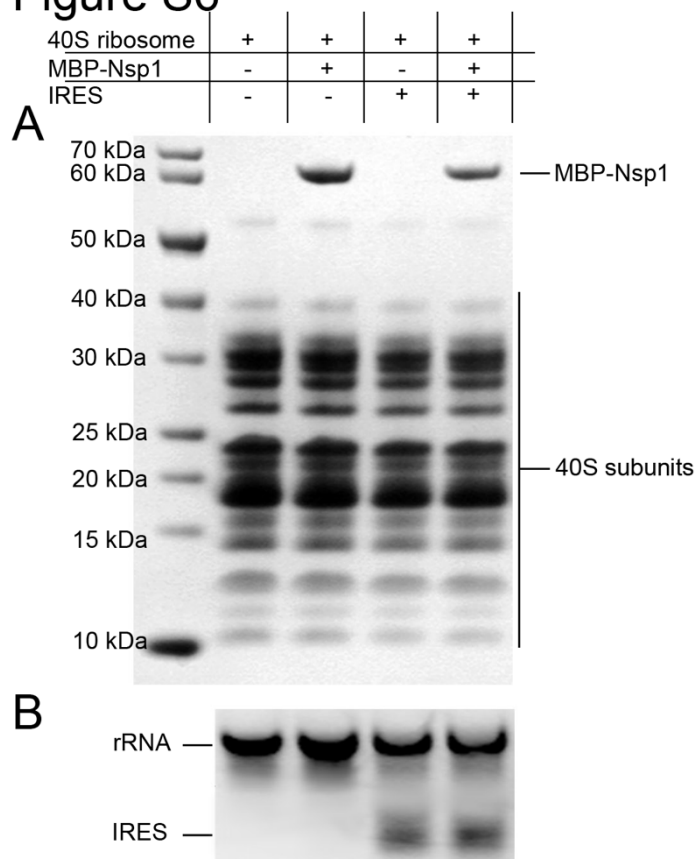


Figure S5



1113

Figure S6



1114

Figure S7

